TEMPO Formaldehyde Retrieval Algorithm Theoretical Basis Document

Gonzalo González Abad[1], Caroline R. Nowlan[1], Xiong Liu[1], Huiqun Wang[1] and Kelly Chance[1]

[1]Center for Astrophysics | Harvard & Smithsonian

Corresponding author: Gonzalo González Abad (ggonzalezabad@cfa.harvard.edu)

VERSION v1.0

RELEASE DATE February 3, 2025

KEYWORDS
FORMALDEHYDE
TEMPO
VOLATILE ORGANIC COMPOUNDS
NON-METHANE HYDROCARBONS/VOLATILE ORGANIC COMPOUNDS
AIR QUALITY
ATMOSPHERIC CHEMISTRY

REVIEWERS Hyeong-Ahn Kwon (University of Suwon) & Eleanor Waxman (CIRES, NOAA)

DOI 10.5067/OQ95W53OG5J4

Table of Contents

Abstract

This Algorithm Theoretical Basis Document (ATBD) describes the retrieval algorithm and product details for the TEMPO Level 2 formaldehyde (HCHO) product. TEMPO is the first air quality mission dedicated to measuring atmospheric trace gases and aerosols over North America from geostationary orbit. The HCHO product is produced using a three-step process. First, the retrieval algorithm derives the differential slant column density of HCHO from backscattered solar light and calculated radiance reference spectra. Second, the algorithm calculates an air mass factor that describes the light path through the atmosphere in order to convert the differential slant column density to a vertical column density. In the third step, the background correction corrects the retrieved columns accounting for the HCHO signal present in radiance reference spectra. The ATBD describes the version 3 HCHO data product's retrieval algorithm, algorithm inputs and outputs, uncertainties and practices for best use.

Plain Language Summary

TEMPO (Tropospheric Emissions: Monitoring of Pollution) is a satellite mission in geostationary orbit that measures trace gases, clouds and aerosols of importance to air quality. This document describes the retrieval algorithm and product details for the TEMPO Level 2 formaldehyde (HCHO) product.

Version

This is Version 1.0 (initial release) of the TEMPO formaldehyde ATBD

1. Introduction

1.1. TEMPO Overview

TEMPO is NASA's first Earth Venture Instrument (EVI-1) project, selected in 2012. It is a PI-led instrument project at the Smithsonian Astrophysical Observatory (SAO) with project management at NASA Langley Research Center (LaRC) and instrument development at Ball Aerospace (now BAE Systems, Inc). TEMPO is NASA's first payload to be hosted on a commercial spacecraft. After the TEMPO instrument delivery in November 2018, the TEMPO mission partnered with the satellite provider Maxar in 2019 and the host IntelSat in 2020. The TEMPO instrument was launched April 7, 2023 from Cape Canaveral on board the commercial geostationary communication satellite IntelSat-40e (IS-40e) by a SpaceX Falcon 9 rocket into a geostationary orbit (GEO) at 91°W. TEMPO's first direct Sun observation took place August 1, 2023, followed by the first Earth-view observations on August 2, 2023. TEMPO began nominal operations on October 17, 2023.

TEMPO uses the UV/visible spectroscopic technique to measure atmospheric pollution across North America, from Mexico City/Puerto Rico to the Canadian oil sands, and from the Atlantic to the Pacific, hourly and at high spatial resolution. Measurements are made from geostationary orbit, which allows for nearly continuous daylight monitoring to capture the inherent high temporal variability in pollutants due to emissions, chemistry and meteorology. A small spatial footprint resolves pollution sources at a sub-urban scale.

TEMPO measures the spectra required to retrieve the mission baseline data products of total and profile ozone (O_3), nitrogen dioxide (NO_2), formaldehyde (HCHO), and cloud fraction and cloud pressure. In addition, TEMPO spectra can also be used to derive sulfur dioxide (SO_2), bromine monoxide (BrO), glyoxal ($C_2H_2O_2$), water vapor (H_2O), nitrous acid (HNO_2), aerosols and Ultraviolet B (UVB) radiation. TEMPO thus can measure the major constituents, directly or by proxy, involved in tropospheric O_3 chemistry, as well as several other tropospheric and stratospheric constituents. TEMPO observations combining ultraviolet and visible wavelengths provide sensitivity to O_3 in the lowermost troposphere, significantly reducing uncertainty in air quality modeling and prediction. TEMPO provides air quality products disseminated to the public via the Atmospheric Science Data Center (ASDC) at NASA LaRC.

TEMPO makes the first tropospheric trace gas measurements from GEO over North America by building upon the heritage of previous spectrometers operating in low-earth-orbit (LEO): GOME (Burrows, et al., 1999), SCIAMACHY (Bovensmann, et al., 1999), OMI (Levelt et al., 2006), GOME-2 (Munro et al., 2016), OMPS (Flynn et al., 2014) and TROPOMI (Veefkind et al., 2012), as well as the GEMS instrument (Kim et al., 2020), launched into GEO in 2020 to measure air pollutants over eastern Asia. These legacy instruments have demonstrated the technologies necessary to provide the measurement precision required for TEMPO using very similar retrieval algorithms. Novel to the GEO missions are hourly measurements with finer spatial resolution. The observational strategy makes TEMPO an innovative application of well-proven techniques, producing a revolutionary dataset for air quality and climate applications.

1.2. TEMPO Instrument and Measurements

Table 1 shows key characteristics of the TEMPO instrument and nominal hourly measurements. More instrument details can be found in Zoogman et al. (2017), and TEMPO

Level 1B Algorithm Theoretical Basis Document (Chong et al., 2025). The TEMPO instrument is a UV/visible imaging grating spectrometer using two 2-D 2k × 1k charge coupled device (CCD) detectors in one focal plane covering the two bands ~293-494 nm (referred to as the UV band) and ~538-741 nm (visible band). The 2k (2048) dimension is for the spatial direction and the 1k (1028) dimension is for the spectral direction. The TEMPO instrument slit aligns in the North/South (N/S) direction and simultaneously measures 2048 (N/S or cross-track) spatial pixels, of which 2036 pixels have good performance. Each band has 1028 spectral pixels, of which ~1016 pixels have good performance. The spectral resolution is ~0.6 nm at Full Width at Half Maximum (FWHM) and the spectral sampling is ~0.2 nm.

Table 1. *TEMPO instrument and measurement characteristics*

Volume, Mass	1.4 m × 1.1 m × 1.2 m, 137 kg
Average operating power	138 W
Detector size	Two 2048 (spatial) × 1028 (spectral) detectors
Wavelength range	UV band: ~293 - 494 nm, Visible band: 538 - 741 nm
Spectral resolution	~0.6 nm @ FWHM (0.54-0.63 nm)
Spectral sampling	~0.2 nm or ~3 pixels / FWHM (2.7-3.2 nm)
Spectral co-registration[1]	< 0.1 pixel (for UV, visible, UV/visible)
Orbit	Geostationary (35786 km), 91.0°W above the Equator
Instantaneous field of view[2]	41.49 µrad (N/S) × 129.20 µrad (E/W)
Modulation Transfer Function @Nyquist[2]	0.31-0.41 (N/S) × 0.38-0.49 (E/W)
Field of view[2,3]	4.87° (N/S) × 8.66° (E/W)
Spatial resolution[2]	2.0 km (N/S) × 4.75 km (E/W) at center of field of regard (FOR) (33.5231° N, 89.2170° W)
Temporal resolution[4]	~1 hour, ~3-second snapshot per mirror step
Spectra per hour [2,3,4,5]	2036 (N/S) × 1181 (E/W)
Maximum Signal-to-Noise Ratio[6]	1372 – 1394 at 330 - 340 nm

[1]Smile (mapping of the same wavelength to different pixels of the focal plane for different spatial columns), keystone (deviation of signal mapping from the correct spatial channel across the focal plane), and UV/visible co-alignment are within 0.1 pixel
[2]N/S represents the North/South (cross-track) direction; E/W represents the East/West (mirror step) direction.

[3]*Estimated with a 128 µrad E/W mirror step size (1.2 µrad overlapping between 2 steps) and 1181 steps*
[4]*For the nominal mode. In the early morning or late afternoon, optimized mode can measure the daylight portion every ~40 minutes. Special modes can measure a selected portion of Field of Regard (FOR) every 5-10 minutes*
[5]*2036 out of 2048 spatial pixels are valid pixels*

[6]*For the nominal radiance without pixel binning, derived using in-flight data from September 1, 2023*

TEMPO can make three types of measurements: Earth-view radiance, solar irradiance, and dark current measurements. The Calibration Mechanism Assembly (CMA) controls the instrument aperture via a wheel with four selectable positions (open, closed, working diffuser, reference diffuser). The two diffusers allow recording of the top-of-atmosphere solar irradiance. The working diffuser is used on a more frequent (e.g., weekly) basis, and the reference diffuser used every 3-6 months to assess trends in degradation of the working diffuser from radiation exposure and contamination. Solar measurements may be made when the Sun is unobscured within 30° to the instrument boresight during night. Earth-view radiance measurements are made in an open position during the daytime. Dark current data are collected with the wheel in the closed position a few times per day, before and after the Earth-view and before the solar measurements.

In a typical day, the TEMPO scan pattern includes optimized scanning in the early morning and late afternoon/evening, and nominal hourly scanning during the middle of the day. A TEMPO nominal hourly scan samples the entire field of regard (FOR) from East to West within 1 hour in 1181 mirror steps. The early morning and late afternoon/evening optimized scans increase the temporal sampling of the sunlit portion of the FOR to every 40 minutes by skipping observations over the dark parts of the continent. Observations of hourly scans are split into 9 granules; each granule includes ~6.7 minutes of data. Due to the fixed Instantaneous Field of View (IFOV), the footprint size on the ground depends on the viewing zenith angle. The footprint is ~2.0 × 4.75 km^2 at the center of the FOR, with an area varying from 8 km^2 over Mexico City to 21 km^2 over the Canadian oil sands. In addition to performing standard operations, TEMPO can use up to 25% of the observation time to perform special observations in high-time scan mode, scanning a selected portion of the FOR (i.e., N/S strip) at much higher temporal resolution (e.g., 5-10 minutes). Special observations can alternate with nominal hourly scans (e.g., 1-hour special observation followed by 1-hour nominal scan of FOR).

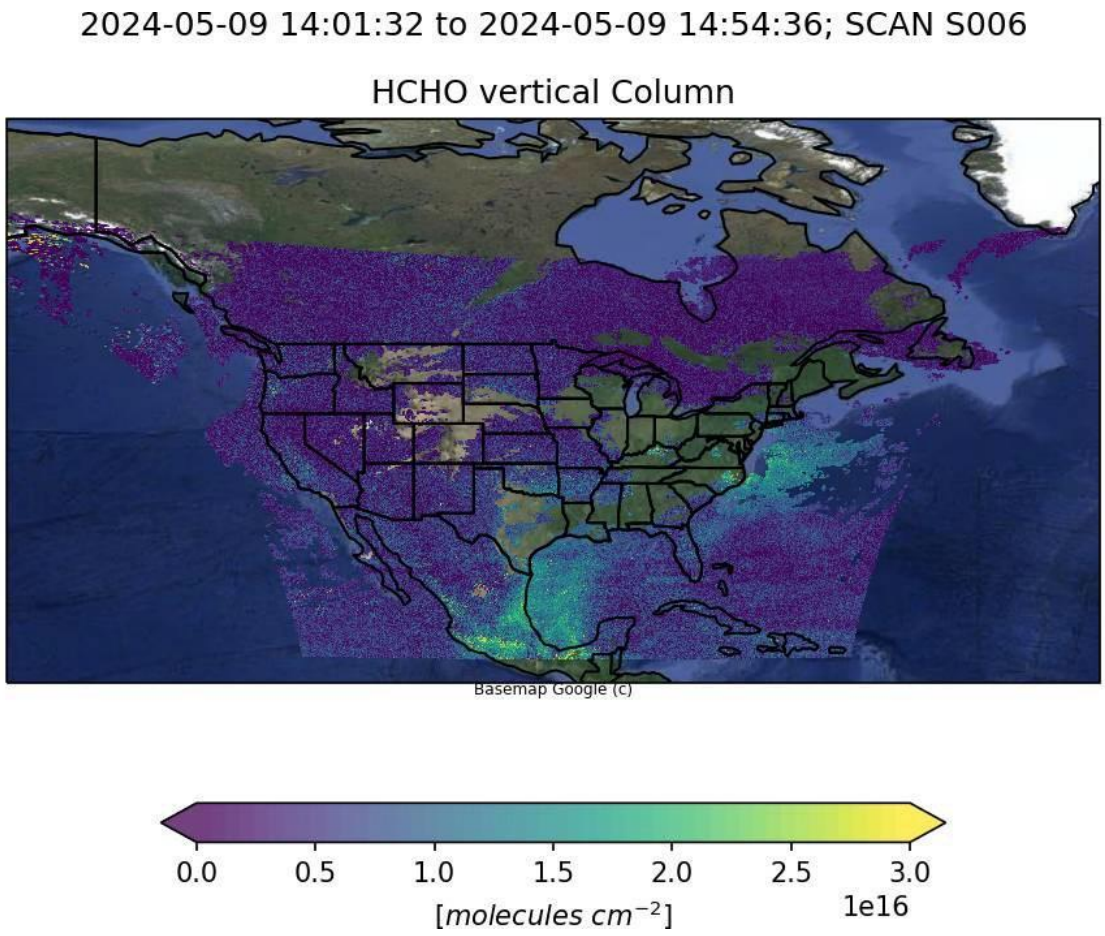

Figure 1. *HCHO vertical column densities retrieved from TEMPO spectra observed on May 9, 2024, scan #6. Due to the large uncertainties and spurious signals of HCHO retrievals over clouds, observations with cloud fraction larger than 0.5 have been masked to avoid misinterpretation.*

1.3. Formaldehyde

Figure 1 shows formaldehyde (HCHO) retrievals from a typical hourly scan of TEMPO's field of regard. Formaldehyde is an important ambient trace gas chemical in the atmosphere. Background levels of HCHO are produced by the oxidation of methane (CH_4) (Munger et al., 1995) while higher concentrations are often produced by the oxidation of precursor gases (volatile organic compounds, VOCs) of anthropogenic (Zhu et al., 2014), biogenic (Zhang et al., 2018) and pyrogenic origins (Alvarado et al., 2020). For example, the largest source of atmospheric HCHO is production by the oxidation of isoprene released from vegetation (Lee et al., 1998). Direct anthropogenic emissions can sometimes also contribute to regional enhancements (Chan Miller et al., 2017).

Formaldehyde plays an important role in the oxidative capacity of the atmosphere. Its photolysis and oxidation contribute to the removal of hydroxyl (OH) and production of hydroperoxyl (HO_2) radicals, and affect the processes governing tropospheric ozone production (Duncan et al., 2014). It also plays an important role in the secondary production of aerosols

(Calvert et al., 2015). HCHO can be directly detrimental to human health since it is reactive to the upper airways and can cause irritation to the eyes, nose and throat (Kim et al., 2019; Swenberg et al., 2013). Given HCHO's short lifetime of a few hours (Logan et al., 1981), satellite observations of HCHO can be used as a proxy for the non- methane VOC emissions that contribute to tropospheric ozone production. For all these reasons, it is important to monitor HCHO to evaluate the oxidative capacity of the atmosphere, quantify its concentration globally, identify and monitor sources and quantify its effects on human health.

2. Context/Background

2.1. Historical Perspective

2.1.1. Formaldehyde Measurements from Space

TEMPO evolved from the 2007 Earth Science Decadal Survey (National Research Council, 2007) GEO-CAPE mission (Fishman et al., 2012) for atmospheric chemistry and ocean color measurements from geostationary orbit, which recommended measurements of O_3, NO_2, SO_2, HCHO, $C_2H_2O_2$ and aerosols from an ultraviolet/visible (UV/Vis) component. TEMPO was designed to achieve as much as possible of the GEO-CAPE atmospheric UV/Vis measurement capability within the cost constraints of the NASA Earth Venture Program.

TEMPO benefits from the heritage of a long history of sensors flown in low Earth orbit (LEO). Formaldehyde was first observed from space using GOME (Chance et al., 2000; Thomas et al., 1998). Since then, it has been successfully retrieved using GOME (De Smedt et al., 2008), SCIAMACHY (De Smedt et al., 2008; Wittrock et al., 2006), GOME-2 (De Smedt et al., 2012), OMI (De Smedt et al., 2015; González Abad et al., 2015), OMPS (González Abad et al., 2016; Li et al., 2015; Nowlan et al., 2023), TROPOMI (De Smedt et al., 2018), and EMI (Su et al., 2022) instruments flying onboard LEO satellites. More recently, GEMS (Kwon et al., 2019; Lee et al., 2024) has provided HCHO observations from a GEO orbit for the first time. The Sentinel-4/UNV instrument is expected to launch into geostationary orbit in 2025, from where it will make HCHO measurements over Europe and North Africa. Together, GEMS, TEMPO and Sentinel-4/UVN form the first geostationary constellation of air quality sensors.

Over the years, satellite HCHO retrievals have enabled researchers to explore multiple aspects of atmospheric chemistry and its interactions with the biosphere. For example, satellite HCHO observations have been used to quantify biogenic emissions and secondary production from isoprene (Barkley et al., 2013; Bauwens et al., 2016; Marais et al., 2012; Stavrakou, Müller, De Smedt, et al., 2009), estimate HCHO impact on secondary aerosol production (Marais et al., 2016), calculate NOx to volatile organic compound ratios to evaluate ozone production regimes (Duncan et al., 2014; Jin et al., 2017; Souri et al., 2020; Valin et al., 2016), derive decadal trends of HCHO in the atmosphere (Barkley et al., 2017; De Smedt et al., 2015; Zhu, Mickley, et al., 2017), estimate the global distribution of OH radicals (Wolfe et al., 2019), evaluate HCHO and VOCs anthropogenic emissions (Zhu et al., 2014), assess cancer risks associated to HCHO surface concentrations (Zhu, Jacob, et al., 2017) and study fire emissions (Alvarado et al., 2020; Stavrakou, Müller, Smedt, et al., 2009).

2.1.2. Algorithm Heritage

The TEMPO HCHO retrieval algorithm has its heritage in the trace gas retrieval algorithms used by the SAO to produce the OMI operational data products OMHCHO (HCHO) (González Abad et al., 2015), OMBRO (BrO) (Suleiman et al., 2018) and OMOCLO (OClO). These algorithms are also used to produce OMI research products glyoxal (Chan Miller et al., 2014; Kwon et al., 2024) and water vapor (Wang et al., 2019). The OMI algorithms are derived from algorithms originally developed for GOME (Chance et al., 2000; Martin et al., 2002). Besides OMI, these algorithms have been applied to retrieve a range of trace gases from several satellite instruments, including GOME-2 (Nowlan et al., 2011), SCIAMACHY (Parrella et al., 2013; Sioris et al., 2004), OMPS (González Abad et al., 2016; Nowlan et al., 2023) and the

airborne instruments ACAM (Liu et al., 2015), GCAS (Nowlan et al., 2018), and GeoTASO (Nowlan et al., 2016). In addition to its heritage in SAO retrieval algorithms, the TEMPO HCHO retrieval algorithm also has heritage in NASA GSFC's operational NO_2 product OMNO2 (Lamsal et al., 2021), included through the TEMPO O2-O2 cloud algorithm (Wang et al., 2025) and the use of geometry-dependent surface Lambert equivalent reflectivity (GLER) (Fasnacht et al., 2019; Qin et al., 2019).

2.1.3. Algorithm Overview and Implementation

TEMPO data products are generated by the SDPC at the Smithsonian Astrophysical Observatory and then pushed to NASA Atmospheric Science Data Center for public distribution. These products include Level 1B spectra (calibrated solar irradiance and geolocated Earth-view radiances), Level 2 trace gas and cloud products (at the native ground pixel footprint for the East-West granules that make up a TEMPO scan) and Level 3 trace gas and cloud products (Level 2 data sampled on a regular grid for all granules constituting a single East-West scan).

The SDPC generates the TEMPO products in the following order from Level 0 (raw data): 1) Level 1B; 2) Level 2 clouds; 3) Level 2 trace gases; and 4) Level 3 products. This order is required because the trace gas products are derived from the Level 1B spectra, and also require the cloud fraction and pressure for the derivation of air mass factors used in their vertical column density calculations.

2.1.4. Product Version

This document describes the TEMPO version 3 HCHO product produced through the SDPC operational processing pipeline. The version 3 product was initially released to the public on May 20, 2024. Updates to the TEMPO operational pipeline result in periodic new data releases. The TEMPO trace gas and cloud user guide (González Abad et al., 2024) provides additional information on versioning history, data format and usage recommendations. The following table describes the major public data releases and algorithm updates.

Table 2. *Product and Science Data Processing Center pipeline versions for public data releases.*

Product Version Designation	**Science Data Processing Center Pipeline Version**	**Release Date**	**Significant Algorithm Updates**
V03	4.4	May 20, 2024	First major public release

2.2. Additional information

2.2.1. List of Acronyms

Table 3. *List of acronyms and abbreviations*

Acronym/Abbreviation	Definition
ACAM	Airborne Compact Atmospheric Mapper
AEROMMA	Atmospheric Emissions and Reactions Observed from Megacities to Marine Areas
AMF	Air mass factor
AQS	Air Quality System
ASDC	Atmospheric Science Data Center
ATBD	Algorithm theoretical basis document
CCD	Charge-coupled device
CCI	Climate Change Initiative
CMA	Calibration Mechanism Assembly
CMAQ	Community Multiscale Air Quality
CUPiDS	Coastal Urban Plume Dynamics Study
DEM	Digital elevation model
DU	Dobson Unit
E/W	East/West
EMI	Environment Monitoring Instrument
EOL	End of life
EPA	Environmental Protection Agency
ERS-2	European Remote-Sensing Satellite-2
EVI	Earth Venture Instrument
FOR	Field of regard
FWHM	Full-width at half maximum
GCAS	GeoCAPE Airborne Simulator
GEMS	Geostationary Environment Monitoring Spectrometer

Acronym/Abbreviation	Definition
GEO	Geostationary orbit
GEO-CAPE	Geostationary Coastal and Air Pollution Events
GEOS	Goddard Earth Observing System
GEOS-CF	GEOS composition forecast
GEOS FP-IT	GEOS Foreward Processing Instrument Teams
GeoTASO	Geostationary Trace gas and Aerosol Sensor Optimization
GLER	Geometry-dependent surface Lambert equivalent reflectivity
GMAO	Global Modeling and Assimilation Office
GMTED2010	Global Multi-resolution Terrain Elevation Data 2010
GOME	Global Ozone Monitoring Experiment
GSFC	Goddard Space Flight Center
HEMCO	Harmonized Emissions Component
HTAP	Hemispheric Transport of Air Pollution
IAGOS	In-service Aircraft for Global Observing System
IFOV	Instantaneous Field of View
IMS	Interactive Multisensor Snow and Ice Mapping System
IS	Intelsat
LaRC	Langley Research Center
LEO	Low Earth orbit
LUT	Look up table
MEGAN	Model of Emissions of Gases and Aerosols from Nature
MINDS	Multi-Decadal Nitrogen Dioxide and Derived Products from Satellites
MODIS	Moderate Resolution Imaging Spectroradiometer
N/S	North/South
NASA	National Aeronautics and Space Administration
NDACC	Network for the Detection of Atmospheric Composition Change

Acronym/Abbreviation	Definition
NEC-AQ-GHG	Northeast Corridor Air Quality and Greenhouse Gas
NOAA	National Oceanic and Atmospheric Administration
OMBRO	OMI bromine monoxide level 2 product
OMHCHO	OMI formaldehyde level 2 product
OMI	Ozone Monitoring Instrument
OMNO2	OMI nitrogen dioxide level 2 product
OMOCLO	OMI chlorine dioxide level 2 product
OMPS	Ozone Mapping and Profiler Suite
PGN	Pandonia Global Network
PI	Principal Investigator
PLRA	Program Level Requirements Appendix
PROFOZ	OMI ozone profile level 2 product
QA4ECV	Quality Assurance for Essential Climate Variables
QFED	Quick Fire Emission Database
RETRO	REanalysis of the TROposhperic chemical composition)
SAO	Smithsonian Astrophysical Observatory
SCD	Slant column density
SCIAMACHY	SCanning Imaging Absorption spectroMeter for Atmospheric CHartographY
SDPC	Science Data Processing Center
SOA	Secondary organic aerosol
SNR	Signal-to-noise ratio
STAQS	Synergistic TEMPO Air Quality Science
Suomi NPP	Suomi National Polar-orbiting Partnership
STAQS	Synergistic TEMPO Air Quality Science
TEMPO	Tropospheric Emissions: Monitoring of Pollution
TOA	Top of atmosphere

Acronym/Abbreviation	Definition
TROPOMI	TROPOspheric Monitoring Instrument
US	United States
UV	Ultraviolet
UVB	B ultraviolet
VCD	Vertical column density
VLIDORT	Vector LInearized Discrete Ordinate Radiative Transfer
VOC	Volatile Organic Compound
WRF-Chem	Weather Research and Forecasting - Chemistry

2.2.2. List of Symbols

Table 4. *List of symbols used in mathematical equations.*

Meaning	**Symbol**
Albedo	α
Albedo (cloud)	α_c
Albedo (snow)	α_s
Albedo (snow free surface)	α_f
Altitude	z
Air mass factor	AMF
Cloud fraction (effective)	f_{ce}
Cloud fraction (radiative)	f_{cr}
Cloud pressure	p_c
Covariance matrix of measurement errors	$\mathbf{S}_\epsilon$
Earth's surface gravity acceleration	g
Gas constant of dry air	R
Gas partial column	n
Hybrid sigma-pressure vertical grid: first Eta coefficient	eta_a
Hybrid sigma-pressure vertical grid: second Eta coefficient	eta_b
Look-up table variables for radiances and scattering weights	I_0, I_1, I_2, I_r, S_b
Model parameters spectral fit	$\mathbf{b}$
Modeled radiance spectrum	$\mathbf{F}$

Observed radiance spectrum	$\mathbf{y}$
Profile shape factor	S
Relative azimuth angle	ϕ
Retrieval state vector for spectral fit	$\mathbf{x}$
Scattering weight	W
Scattering weight: clear sky	W_{clear}
Scattering weight: cloudy sky	W_{cloud}
Slant column density	SCD
Snow/ice fraction	f_s
Solar irradiance	I_0
Solar zenith angle	θ_0
Super-Gaussian normalization factor	A_s
Super-Gaussian asymmetry parameter	a_q
Super-Gaussian exponent (shape) parameter	k
Super-Gaussian instrument line shape function	s
Super-Gaussian width parameter	q
Surface pressure	p_s
Surface temperature	T_s
Temperature	T
Temperature correction factor	c

Temperature lapse rate	Γ
Terrain altitude	h
TOA radiance	I
TOA radiance (clear sky)	I_{clear}
TOA radiance (cloudy sky)	I_{cloud}
Vertical column density	VCD
Viewing zenith angle	θ
Wavelength	λ

2.2.3. Chemical Expressions

Table 5. *List of chemical formulas*

Meaning	**Formula**
Bromine monoxide	BrO
Chlorine dioxide	$OClO$
Formaldehyde	$HCHO$
Glyoxal	$C_2H_2O_2$
Hydroperoxyl	HO_2
Hydroxyl	OH
Iodine Oxide	IO
Nitric oxide + nitrogen dioxide	NO_x
Nitrogen dioxide	NO_2

Nitrous acid	HNO_2
Molecular oxygen	O_2
Molecular oxygen collision complex	O_2-O_2
Ozone	O_3
Sulfur dioxide	SO_2
Water vapor	H_2O

3. Algorithm Description

3.1. Scientific Theory

3.1.1. Overview

The TEMPO retrieval algorithm used to produce Level 2 HCHO vertical column densities has three major processing steps:

1. Spectral fitting to calculate differential slant column densities (dSCDs)
2. Air mass factor (AMF) calculation for converting SCDs to vertical column densities (VCDs)
3. Background correction to account for HCHO present in the radiance reference spectra

Figure 2 summarizes the major inputs, outputs and processing steps that will be described in this section.

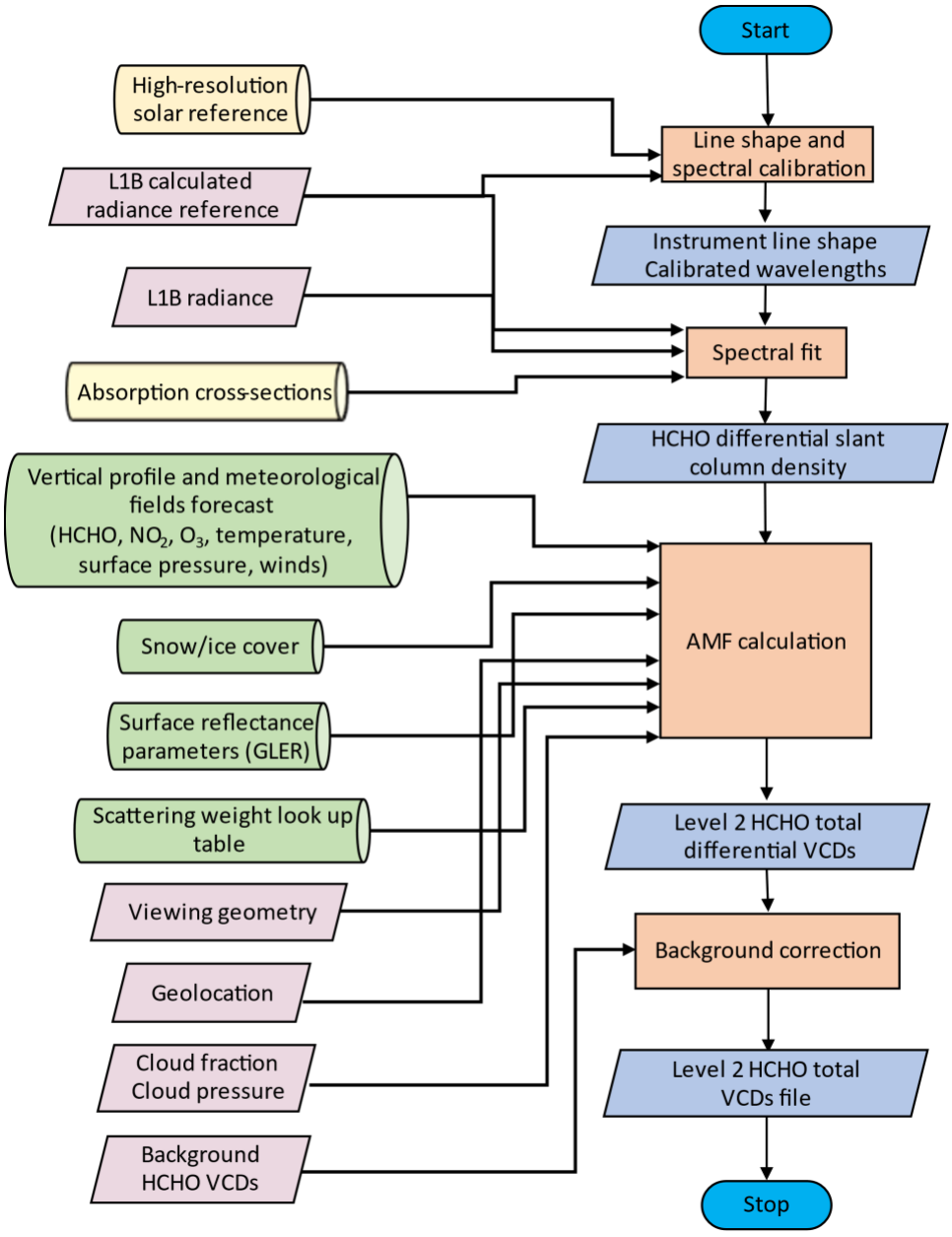

Figure 2. *Flow chart of TEMPO HCHO retrieval algorithm, showing slant column input databases (yellow cylinders), AMF input databases (green cylinders), variable inputs from TEMPO radiance and cloud information (pink parallelograms), algorithm output/inputs (blue parallelograms) and major processing steps (orange rectangles).*

The background corrected vertical column density (VCD) of HCHO is the final product of the retrieval algorithm. It is based on the retrieved dSCDs and the background HCHO slant column densities estimated using GEOS-CF forecast simulations (SCD_{corr}). The product of the spectral fit is dSCDs and not SCD due to the use of a radiance reference as source term (see section 3.1.2.2). The final VCD is related to the sum of the two by

$$VCD = \frac{dSCD + SCD_{corr}}{AMF}$$

(1)

where AMF represents the air mass factor for a given scene. Figure 3 shows an example of HCHO VCDs retrieved with TEMPO's algorithm in the Western part of TEMPO's FOR.

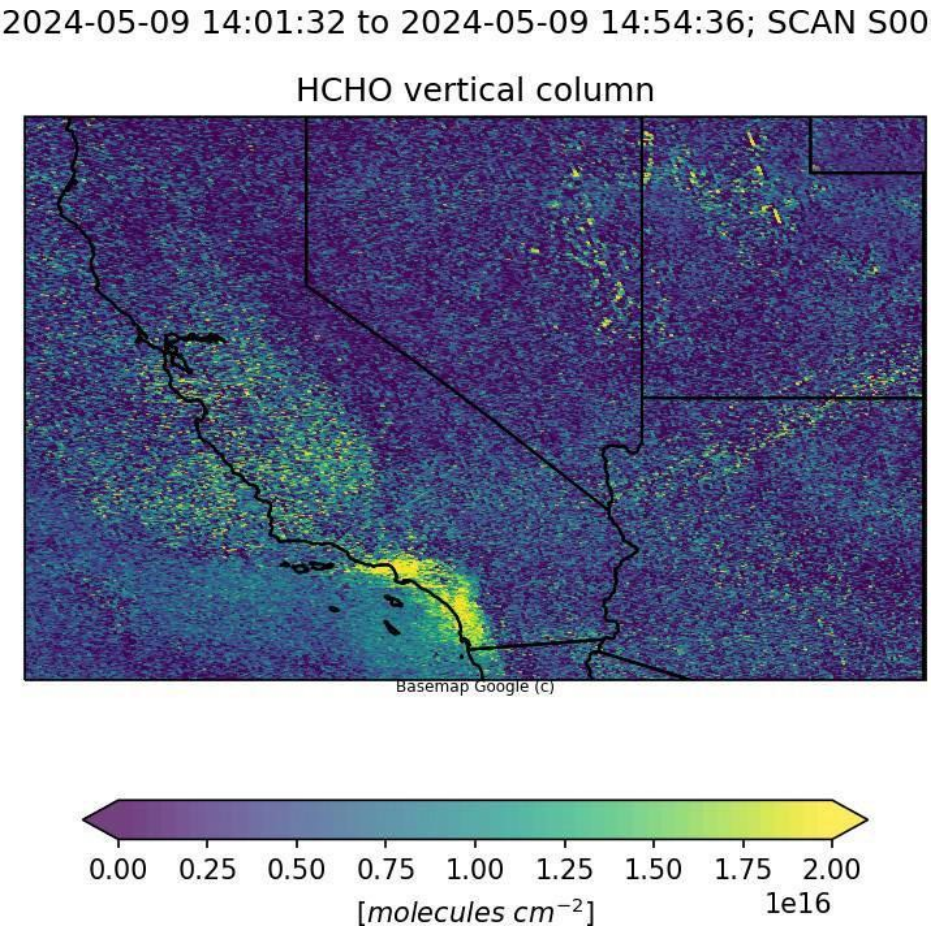

Figure 3. *HCHO VCDs retrieved from TEMPO observations on 9 May 2024, scan #6. The very strong signal over California's southern coast is linked to the presence of clouds. (No cloud filtering has been applied in this image.) The use of HCHO TEMPO retrievals over cloudy scenes is discussed in the algorithm usage section.*

3.1.2. Differential Slant Column Density Retrieval

3.1.2.1 Theoretical Basis for Spectral Fitting

Differential slant columns are derived using least-squares minimization to directly fit a modeled radiance spectrum $\boldsymbol{F(x, b)}$ to an observed radiance spectrum $\boldsymbol{y}$ through non-linear least-squares Levenberg-Marquart minimization of a cost function χ^2:

$$\chi^2 = [y - F(x,b)]^T S_\epsilon^{-1} [y - F(x,b)] \quad (2)$$

where $\mathbf{S}_\epsilon$ is the covariance matrix of measurement errors. In practice, errors on individual

detector pixels in the detector are assumed to be uncorrelated, and $\mathbf{S}_\epsilon$ in the case of this retrieval is a diagonal matrix.

The modeled spectrum is a function of pre-determined model parameters **b** and the retrieved state vector **x**, the set of variables representing the unknow properties of the forward model. The modeled spectrum at each wavelength λ is represented by

$$F(\lambda) = [x_a I_0(\lambda) + b_u(\lambda)x_u + b_r(\lambda)x_r]e^{-\sum_i b_i(\lambda)x_i} \sum_j (\lambda - \underline{\lambda})^j x_j^{SC} + \sum_k (\lambda - \underline{\lambda})^k x_k^{BL} \quad (3)$$

In this equation, I_0 is a radiance reference spectrum (see section 3.1.2.2 for details on its calculation) calculated using Earth-view TEMPO observations scaled by a retrieved intensity parameter x_a (which mainly represents reflectance off the surface or clouds). The term $b_u(\lambda)$ describes a correction for spectral undersampling (Chance et al., 2005), while $b_r(\lambda)$ represents the effects of rotational Raman (Ring) scattering (Chance & Spurr, 1997). The retrieved slant columns for the trace gas of interest (HCHO) and any other spectrally- interfering gases are represented by x_i. Their absorption cross sections, convolved with the instrument line shape and corrected for the "I_0 effect" (Aliwell et al., 2002), are included as $b_i(\lambda)$. The *I_0 effect* accounts for the influence of absorption features in the solar spectrum in the retrieval of absorbing trace gases such as O_3, NO_2, BrO and HCHO. In addition, the retrieval also determines scaling (of order *j*) and baseline (of order *k*) polynomial coefficients (x^{SC} and x^{BL}) that represent low frequency wavelength-dependent effects from surface reflectivity, molecular scattering, aerosols and instrument artifacts. Ideally TEMPO HCHO retrieval would use as I_0 a solar irradiance observed by the instrument near the time prior to the start of Earth-view radiance observations. However, previous experience with HCHO retrievals from LEO and GEO instruments equipped with 2D CCD detectors shows that using a solar irradiance as I_0 term results in large cross track (in the case of TEMPO East/West) stripes (González Abad et al., 2015; Nowlan et al., 2023). In consequence, the retrieval uses a radiance reference instead of the canonical solar irradiance.

3.1.2.2 Radiance Reference Calculation

HCHO retrieval algorithms designed for LEO instruments using 2D CCD detectors have a long heritage of using calculated radiance reference spectra as a source term. These radiance reference spectra are derived using Earth-view TEMPO measurements as described below. A forward model built around a radiance reference spectrum helps to mitigate cross track striping and provides an empirical solution to account for poorly modeled processes. Yet, transferring this approach to TEMPO observations is challenging given the area sampled and the observation geometries of TEMPO. Best practices to calculate TEMPO radiance reference spectra are under investigation at the time of writing this ATBD. Substantial modifications to the methodology described here are expected in a future data release.

LEO missions leverage observations over the remote Pacific Ocean, where background HCHO concentrations are easy to model and homogeneous, to calculate radiance reference spectra. Unfortunately, TEMPO's FOR does not contain such a "clean" area, complicating the

quantification of background concentrations and the selection of Earthshine radiance spectra with small HCHO signatures. Another factor adding complication to the radiance reference calculation is the presence of clouds, which introduce interfering spectral signatures in the HCHO retrieval.

The v3 TEMPO HCHO retrieval algorithm calculates one radiance reference for each cross track position for each TEMPO scan and stores it for later use. The radiance reference for a given cross track position is calculated as the mean of all the radiances in one scan for that cross track position after excluding pixels where:

- Cloud fraction is greater than 0.5.
- The radiances deviate more than one standard deviation from the median radiance for the whole scan.
- Any bit of the Level 1B spectral quality flags (pixel_quality_flag in Level 1B file) is set.

From the set of radiance reference calculations archived, the retrieval pipeline selects the closest one available (date and time considered separately) to proceed with the retrieval of differential slant column densities.

3.1.2.3 Spectral Calibration Using On-Orbit Data

Prior to the main spectral fitting, the TEMPO instrument line shape is derived, and the detector-pixel-to-wavelength spectral calibration is refined by fitting the calculated radiance reference spectrum to a simulated solar spectrum. The simulated solar spectrum is calculated by convolving a high-resolution reference spectrum (Coddington et al., 2023) with the instrument line shape. This step follows a calibration approach used in previous SAO trace gas retrievals (Bak et al., 2017; Sun et al., 2017). The algorithm simultaneously retrieves the solar wavelength registration (using a constant shift from the first-guess wavelengths provided in the Level 1B irradiance) and three terms (width factor q, shape factor k and asymmetry factor a_q) that define the instrument line shape represented by a super-Gaussian function (Beirle et al., 2017)

$$s(\Delta\lambda) = A_s \cdot exp\left[-\left|\frac{\Delta\lambda}{q + sgn(\Delta\lambda)a_q}\right|^k\right] \quad (4)$$

where Δλ is the wavelength distance from the center of the instrument line shape function, A_s is a normalization factor, and sgn() is the sign function used to define the two sides of the instrument line shape. We determine an instrument line shape function for each across-track position of the CCD array using the entire HCHO wavelength window. The line shape parameters are saved for each across-track position, and later applied to all retrievals at that position. Figure 4 shows the results of the spectral calibration against a radiance reference calculated for scan #6 on 9 May 2024.

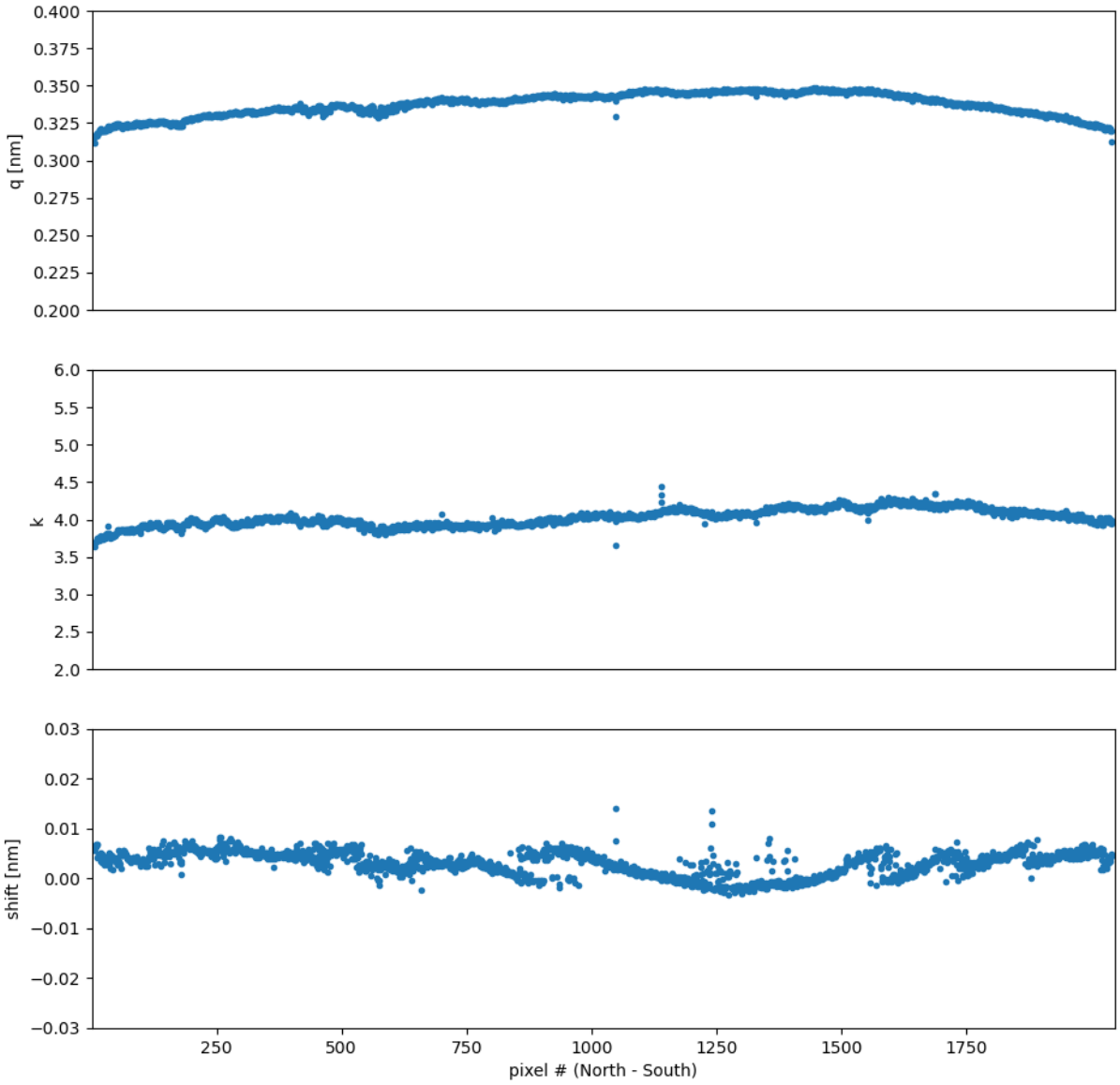

Figure 4. *Spectral calibration results showing half width over e (top panel), shape factor (middle) and the wavelength grid shift (bottom) derived from the HCHO retrieval. As the TEMPO slit functions in the HCHO fitting window show high symmetry, the spectral calibration algorithm sets the asymmetry factor to zero.*

3.1.2.4 Application to Formaldehyde

The HCHO retrieval uses the fitting window 328.5 - 356.5 nm. Table 6 describes the fitting details used for the TEMPO retrievals. The retrieval simultaneously fits slant column densities (x_i) for HCHO, NO_2, O_3, BrO and O_2-O_2, as well as the Ring spectrum magnitude (x_r), scaling (x^{SC}) and baseline (x^{BL}) closure polynomials that account for low-frequency effects (such as Rayleigh and Mie Scattering), a correction for undersampling (x_u), and a wavelength shift which represents the difference in detector pixel wavelength registration between the spectrum of interest and the reference spectrum. The shift in wavelength calibration is typically

due to thermal changes in the instrument over the course of a day, as well as inhomogeneous scene illumination (Noël et al., 2012; Voors et al., 2006). Figure 5 shows an example of the cross sections, and the molecular Ring spectrum used in the retrieval of the HCHO SCD. Figure 6 shows an example of TEMPO HCHO dSCDs retrieved over the region and dates shown in Figure 3.

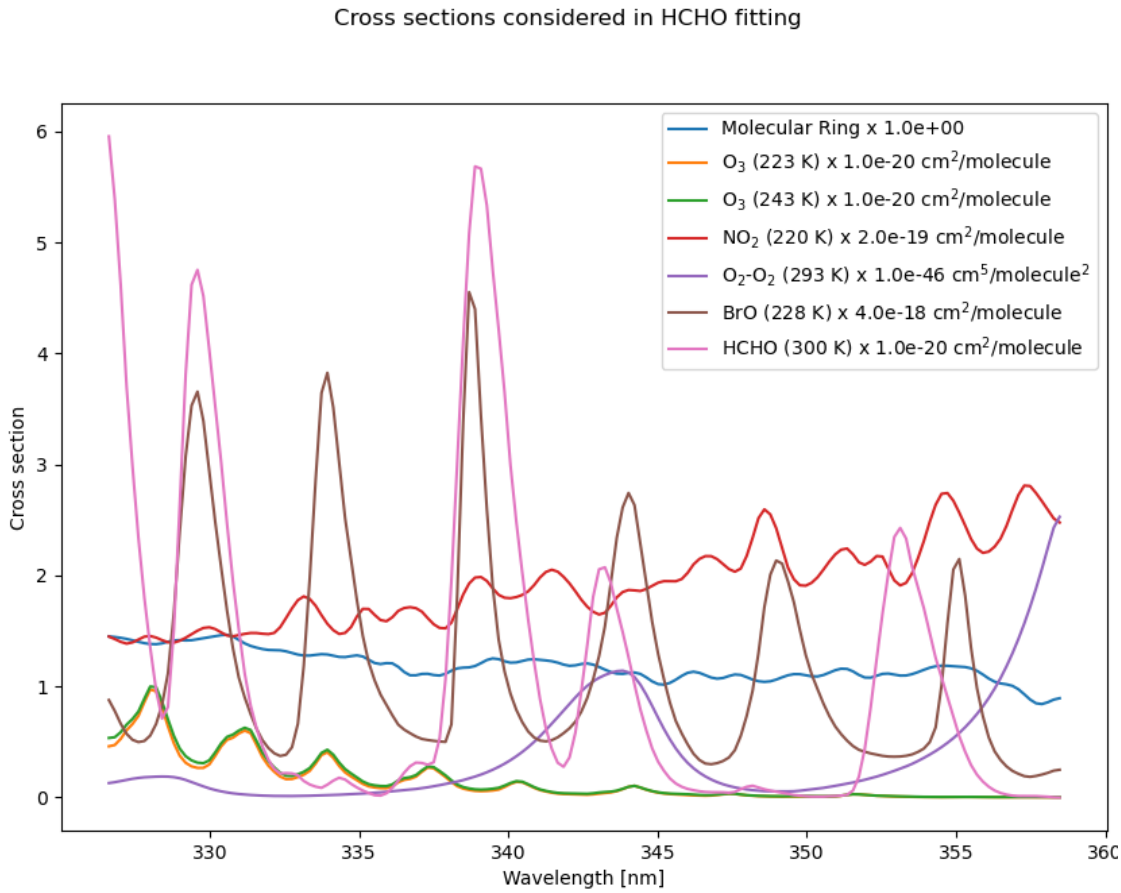

Figure 5. *Cross sections of the molecules and molecular Ring considered in the TEMPO retrievals of HCHO convolved with TEMPO's instrument function at cross track position #1000 on October 6, 2023.*

Table 6. *Parameters fit in TEMPO HCHO slant column density retrieval.*

Parameter	**Details**
HCHO	Chance & Orphal (2011), 300 K
NO_2	Vandaele et al. (1998), 220 K
O_3	Serdyuchenko et al. (2014), 223 and 243 K

BrO	Wilmouth et al. (1999), 228 K
O_2-O_2	Finkenzeller & Volkamer (2022), 293 K
Undersampling	Chance et al. (2005)
Ring effect	Chance & Spurr (1997)
Scaling polynomial	3rd order
Baseline polynomial	3rd order
Wavelength shift	Single value for the entire fitting window

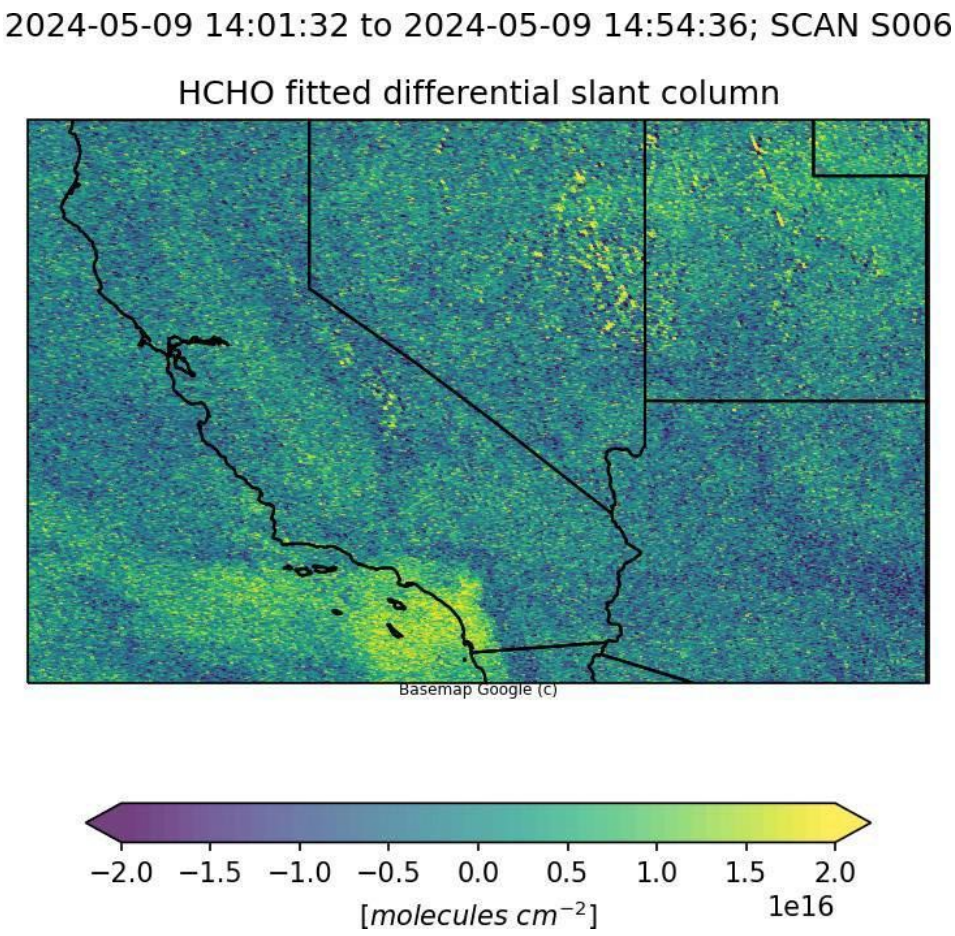

Figure 6. *HCHO dSCDs retrieved from TEMPO observations on May 9 2024, scan #6. The very strong signal over California Southern coast and the "salt and pepper" patterns around the border between Nevada and Utah are linked to the presence of clouds. The use of HCHO TEMPO retrievals over cloudy scenes is discussed in the algorithm usage section.*

3.1.2.5 Treatment of Bad Detector Pixels

The spectral fitting code excludes detector pixels that are flagged in the Level 1B variable *pixel_quality_flag* as "missing_data", "bad_pixel", "processing_error", or "saturated", by de-weighting the detector pixel in the fit. The Level 1B ATBD provides further detail regarding the methodology used to determine the value of the *pixel_quality_flag* in the Level 1B files.

The TEMPO retrieval also employs a "hot pixel" spike removal procedure, which removes the effect of anomalous detector radiance spikes. After spectral fitting, any TEMPO detector pixels that show greater than a given σ deviation (3 times the standard deviation in the case of HCHO) from the mean fitting residual are flagged, and the spectral fitting is repeated excluding those pixels. For LEO instruments, these hot pixels primarily occur due to energetic particles that may impact detectors as satellites pass through the region affected by the South Atlantic Anomaly. Given the novel GEO orbit of TEMPO it is unknown how often these "hot" pixels will appear. Initial analysis suggests a small impact of hot pixels on the retrieval results.

3.1.3. Air Mass Factor Calculation

3.1.3.1 Overview

The air mass factors are calculated on a scene-by-scene basis using the formulation of Palmer et al. (2001) and Martin et al. (2002) for an assumed atmosphere with optically thin absorbers. The photon path is assumed to be constant within the wavelength fitting window, and for HCHO the AMF is determined at 340 nm. The AMF is defined as a function of altitude-dependent scattering weights $W(z)$ and a profile shape factor $S(z)$, each defined from the surface to the top of the atmosphere (TOA), as

$$AMF = \int_{surface}^{TOA} W(z)S(z)dz \tag{5}$$

The profile shape factor is a normalized profile shape, and is calculated from the partial columns of HCHO at each layer, $n(z)$, using

$$S(z) = \frac{n(z)}{\int_{surface}^{TOA} n(z)dz} \tag{6}$$

In the case of operational TEMPO processing, these partial columns are determined from the GEOS-CF chemical transport model, which is described below. Figure 7 shows the AMFs calculated using this formulation for scan #6 on May 9, 2024.

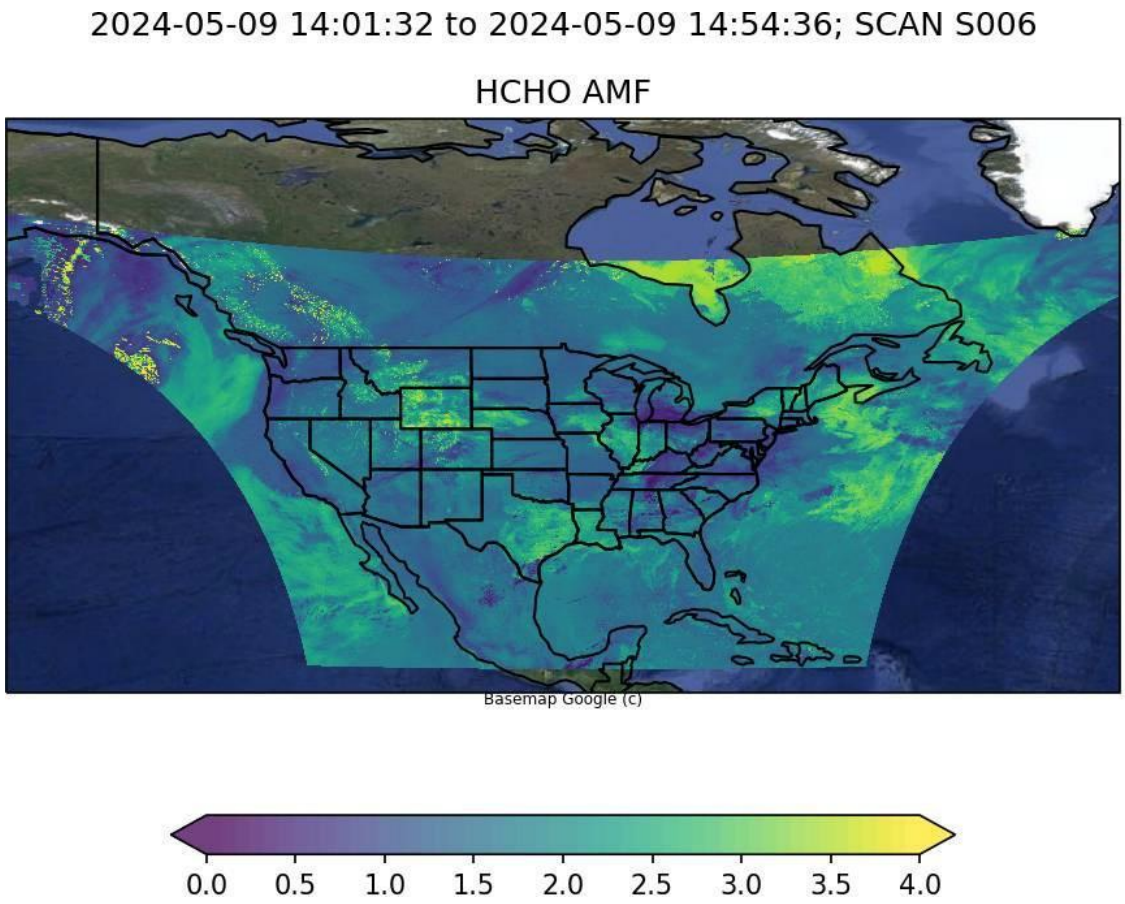

Figure 7. *HCHO AMFs at 340 nm retrieved from TEMPO observations on 9 May 2024, scan #6. The presence of clouds, ice and snow has a large impact on the value of the AMFs. As discussed later, it is important to take these parameters into consideration to filter observations with large uncertainties when using TEMPO HCHO retrievals.*

3.1.3.2 Radiative Transfer Model and Look up Tables

The scattering weight $W(z)$ describes the sensitivity of the HCHO retrieval at different altitudes. $W(z)$ and TOA radiances depend on wavelength, viewing geometry, atmospheric scattering (both Rayleigh molecular scattering and Mie scattering associated with clouds and aerosols) and surface properties. Owing to the computational cost of simulating scattering weights and TOA radiances using radiative transfer models, it is common to use pre-computed look up tables (LUTs). In the case of TEMPO HCHO, the algorithm uses a LUT calculated with version 2.8 of the Vector LInearized Discrete Ordinate Radiative Transfer (VLIDORT) model (Spurr, 2006). The LUT provides information on $W(z)$ and TOA radiances for clear (I_{clear}) and cloudy (I_{cloud}) observations as a function of altitude (z) (expressed as atmospheric pressure), solar zenith angle (θ_0), viewing zenith angle (θ), surface albedo (α), surface pressure (p_s), cloud pressure (p_c) and ozone profile. As described in section 3.1.3.7, aerosols are not explicitly treated in the retrieval. Table 7 summarizes the nodes of the LUT.

The 22 ozone profiles employed in the VLIDORT simulations were derived using OMI ozone profile retrievals (PROFOZ) (Liu et al., 2010). These profiles represent climatological

values for three latitudinal bands: |*latitude*| < 30°for the tropical band (L), 30° < |*latitude*| < 60° for the middle latitude band (M) and |*latitude*| > 60° for the polar latitude band (H). For each latitudinal band several representative ozone total columns were computed. The specific nodes for the LUT interpolation are selected based on the observation latitude and an ozone column derived from the a priori ozone profile (see section below on "Atmospheric Model and Trace Gas Profiles").

To improve computing time, the LUT stores the variables I_0, I_1, I_2, I_r, S_b, dI_0, dI_1 and dI_2 from which linear interpolation can be applied to recover the TOA radiance (I) and scattering weights $W(z)$ using the relative azimuth angle ϕ and albedo α with the following expressions:

$$I = I_0 + I_1 \cdot cos\, cos\,(\phi) + I_2 \cdot cos\, cos\,(2\phi) + \frac{I_r \cdot \alpha}{(1 - \alpha \cdot S_b)} \quad (7)$$

and

$$W(z) = dI_0 + dI_1 \cdot cos\, cos\,(\phi) + dI_2 \cdot cos\, cos\,(2\phi) \quad (8)$$

In equation 7 the first three terms describe the atmospheric component of the radiance, with I_0, I_1 and I_2 being dependent on the solar and viewing zenith angles. The last term in the equation provides the surface contribution, where $I_r \cdot \alpha$ is the direct reflection from a Lambertian surface with albedo α and $(1-\alpha S_b)^{-1}$ represents multiple reflections between the surface and the atmosphere.

Since ozone absorption is not very strong in the HCHO fitting window for solar zenith angles smaller than 70°, the wavelength dependency of $W(z)$ is small. In consequence, only one LUT derived at 340 nm is used. While this simplification introduces some uncertainty in the AMF calculation, those are not larger than 5% (González Abad et al., 2015). For solar zenith angles larger than 70° the assumption of an optically thin atmosphere starts to break down and the derivation of AMFs as described here loses accuracy. Large solar zenith angles occur in the early morning and late afternoon hours of the day. They affect Northern latitudes during the winter months. Retrievals with large solar zenith angles have a main data quality flag of 1 (i.e., suspect, see section 5).

Table 7. *Nodes for TEMPO HCHO LUT. The last three digits of the ozone profile identifiers indicate the total column in Dobson Units (DU). For example, L200 indicates the 200 DU tropical latitude profile.*

Parameter	**Number of nodes**	**Nodes**

Solar zenith angle (θ_0) [degree]	11	0, 15, 30, 45, 55, 65, 70, 75, 80, 85, 89.9
Viewing zenith angle (θ) [degree]	11	0, 15, 30, 45, 55, 65, 70, 75, 80, 85, 89.9
Surface albedo (α)	8	0.0, 0.01, 0.05, 0.1, 0.2, 0.5, 0.8, 1.0
Surface/cloud pressure (p_s/p_c) [hPa]	12	50, 100, 200, 300, 400, 500, 600, 700, 800, 900, 1013, 1050
Ozone profile	22	Tropical latitudes: L200, L250, L300, L350 Middle latitudes: M200, M250, M300, M350, M400, M450, M500, M550 Polar latitudes: H100, H150, H200, H250, H300, H350, H400, H450, H500, H550
Pressure levels [hPa]	47	0, 0.1, 0.2, 0.5, 0.9, 1.3, 2.0, 2.9, 4.4, 6.7, 10.3, 16.0, 25.2, 40.2, 64.6, 100.0, 150.0, 200.0, 250.0, 300.0, 350.0, 400.0, 425.0, 450.0, 475.0, 500.0, 525.0, 550.0, 575.0. 600.0, 625.0, 650.0, 675.0, 700.0, 725.0, 750.0, 775.0, 800.0, 825.0, 850.0, 875.0, 900.0, 925.0, 950.0, 975.0, 1013.0, 1050.0

Figure 8 shows typical scattering weights for clear sky and cloudy pixels alongside GEOS-CF a priori HCHO profiles used to determine shape factors for "clean" and "polluted" scenes (see section 3.1.3.5 for information on the GEOS-CF gas profiles).

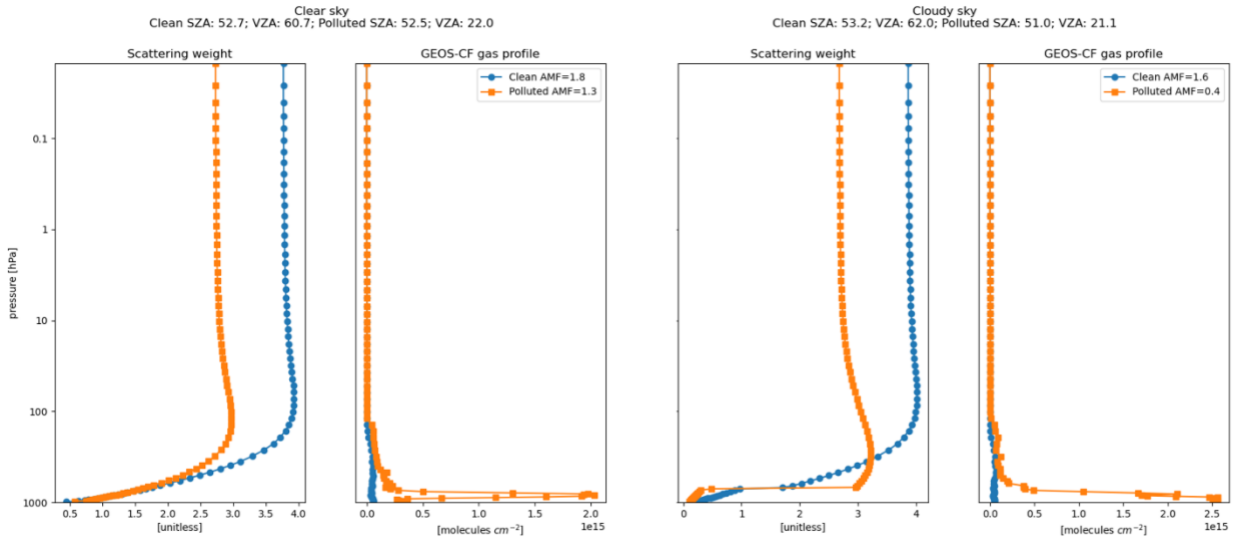

Figure 8. *Sample scattering weights for clear-sky (cloud-free) and cloudy observations, as well as vertical profiles of HCHO partial columns in clean and polluted areas forecasted by GEOS-CF and used in the calculation of four AMFs in TEMPO's granule 5, scan 6 on May 9, 2024. Under polluted conditions (orange lines), the GEOS-CF gas profiles have greatly increased partial columns in the boundary layer (~below 850 hPa) relative to the clean conditions (blue lines). The cloudy sky scattering weights (right half of the figure) show greatly reduced sensitivity below the cloud relative to clear sky conditions (left half of the figure). In both cases, clear and cloudy sky examples, the difference in shape of the clean and polluted scattering weights is linked to different viewing zenith angles.*

3.1.3.3 Clouds

The AMF for a partly cloudy scene is determined using the independent pixel approximation (Martin et al., 2002). In this case it is necessary to calculate the scattering weight for the pixel using the following expression

$$W(z) = (1 - f_{cr}) \cdot W_{clear}(z, \alpha, p_s) + f_{cr} \cdot W_{cloud}(z, \alpha_c, p_c) \quad (9)$$

where $W_{clear}(z, \alpha, p_s)$ is the scattering weight associated with a fully cloud free scene at a particular altitude (z), depending for a given viewing geometry on the surface albedo (α) and the surface pressure (p_s), and $W_{cloud}(z, \alpha_c, p_c)$ is the scattering weight associated with a hypothetical fully cloud covered scene. Clouds are accounted for in the radiative transfer simulation as Lambertian surfaces with an albedo (α_c) of 0.8 placed at the cloud pressure height (p_c). The cloud radiance fraction f_{cr} is defined as

$$f_{cr} = \frac{f_{ce} \cdot I_{cloud}}{(1 - f_{ce}) \cdot I_{clear} + f_{ce} \cdot I_{cloud}} \quad (10)$$

where I_{clear} and I_{cloud} are the TOA radiance intensities determined from the LUT for a completely clear and a completely cloudy scene,

respectively. The scene's effective cloud fraction ($0 \leq f_{ce} \leq 1$) and the cloud pressure are obtained from the TEMPO cloud retrieval product (Wang et al., 2025).

3.1.3.4 Surface Reflectance

For each TEMPO observation, an associated Geometry-dependent surface Lambertian Equivalent Reflectivity (GLER) (Fasnacht et al., 2019; Qin et al., 2019) is calculated. Different GLER derivations are used over land and water. In the version 3 implementation, TEMPO ground pixels are categorized as either land or water using the location of the pixel center. As a result, TEMPO pixels that in reality cover both land and water (i.e., rivers, lakeshores and coastal pixels) do not currently consider mixed surface type GLER.

Over land, the GLER value (albedo) is obtained from two climatologies representing snow free (α_f) and snow covered (α_s) scenes. Using information from the 1-km Interactive Multisensor Snow and Ice Mapping System (IMS) product (U.S. National Ice Center, 2008), a final GLER value that can be used as the albedo (α) is determined by weighting with the snow/ice fraction f_s:

$$\alpha = (1 - f_s) \cdot \alpha_f + f_s \cdot \alpha_s \tag{11}$$

Twenty-two years (2000-2022) of MODIS Bidirectional Reflectance Distribution Function (BRDF) retrievals were used to generate GLER climatologies; the MCD43C1 (Schaaf & Wang, 2015a) and MCD43C2 (Schaaf & Wang, 2015b) v6.1 products are used for snow-covered and snow-free scenes respectively. Using the derived BRDF climatologies, a set of monthly GLER LUTs were created following the approach of Qin et al. (2019). The land GLER LUTs have a resolution of 0.05°×0.05° and cover the region of 15°W to 167°W and 14°N to 73°N. The LUTs represent the variation of the GLER during a day by storing values at each location every 30 minutes. The final GLER value is obtained by linear interpolation to the TEMPO observation time corresponding to the day and month.

In the case of water surface, a single GLER is derived from one set of LUTs constructed using the Cox-Munk slope distribution (Cox & Munk, 1954) as described in Fasnacht et al. (2019). The water GLER LUTs are parameterized as function of wind speed, time of the day and location. They have a resolution of 1°×1° and cover 15°W to 167°W and 14°N to 73°N.

Both sets of LUTs, land and water, are derived at 340 nm for HCHO. The land LUT at this wavelength is derived using a probabilistic model (factor analysis) that estimates the BRDF at a given wavelength using BRDF observations from the first four MODIS bands (Chan Miller et al., 2019). This model is trained on reflectance spectra from the USGS spectral library (Kokaly et al., 2017) and SCIAMACHY LER (Tilstra et al., 2017) following the methodology described by Zoogman et al. (2016). Figure 9 shows an example of the GLER calculated for TEMPO retrievals at 340 nm.

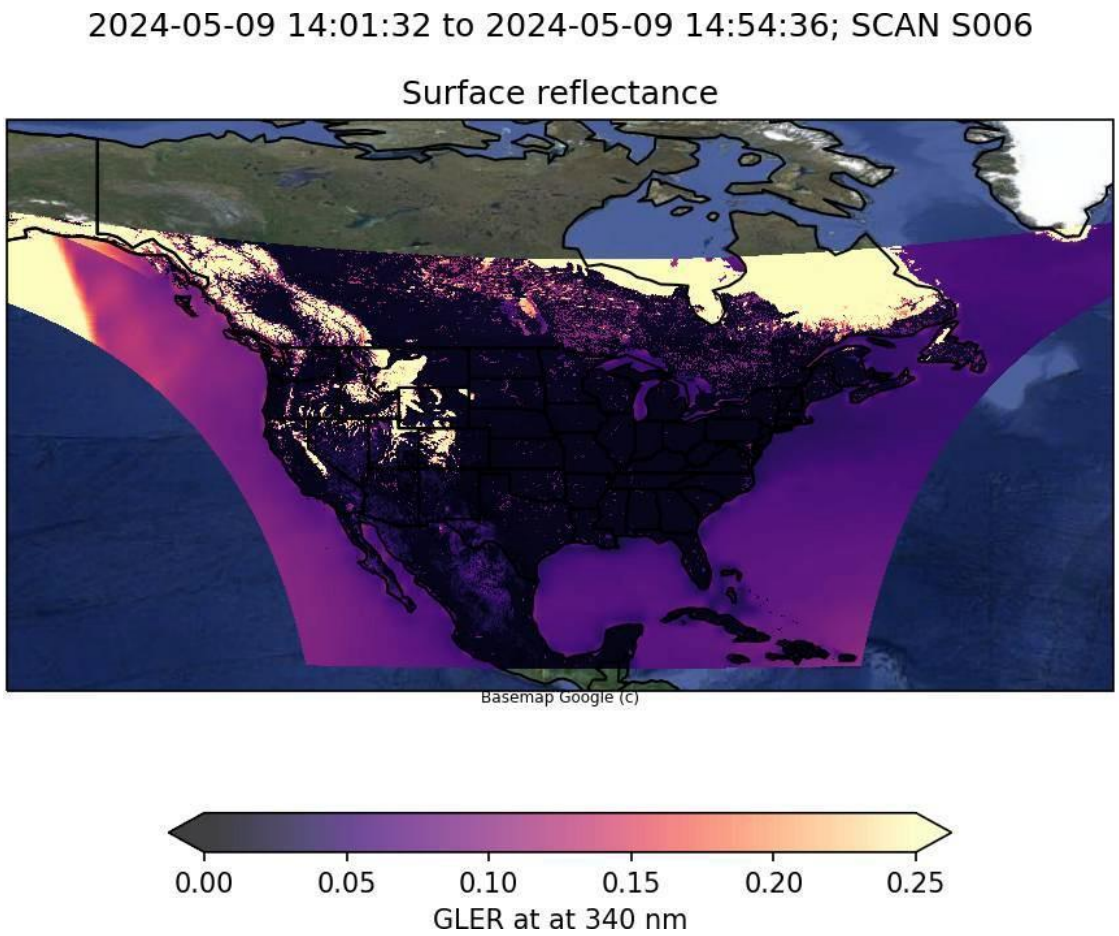

Figure 9. *GLER employed in the calculation of AMFs for TEMPO observations in scan #6, May 9, 2024. A maximum value of 0.25 in the colormap is chosen to facilitate the perception of details over land not covered by snow and ice. The discontinuity over the ocean (Western most part of the domain) is an artifact associated with the node density of the current GLER LUTs.*

3.1.3.5 Atmospheric Model and Trace Gas Profiles

The trace gas algorithm uses atmospheric trace gas profiles and parameters from the Goddard Earth Observing System (GEOS) Composition Forecasting (GEOS-CF) model (Keller et al., 2021; Knowland, Keller, Wales, et al., 2022). GEOS-CF is a chemical forecasting system produced by NASA's Global Modeling and Assimilation Office (GMAO). The GEOS-CF system performs near real-time 5-day forecasts of atmospheric composition using the offline GEOS-Chem chemical transport model (http://geos-chem.org) integrated into the GEOS system. Gases and aerosols are simulated at the same resolution as meteorology on a cubed-sphere at c360 (~25 km) horizontal resolution and 72 vertical layers from the surface to 0.01 hPa. First, this coupled system is run for the previous 24 hours to have the best initial conditions for the global 5-day forecast produced each day at time 12:00 UTC. Output is saved at high temporal frequency (1 hour) and 0.25° latitude × 0.25° longitude as NetCDF files (Knowland, Keller, & Lucchesi, 2022).

Details on the GEOS-CF system and performance of the version 1.0 tropospheric

simulation can be found in (Keller et al., 2021). The stratospheric component of the GEOS-CF is described and evaluated in Knowland et al. (2022). The version 1.0 implementation, emission inventories and outputs are described in Knowland et al. (2022). GEOS-CF version 1.0 uses gas-phase chemistry simulated with GEOS-Chem version 12.0.1. GEOS-Chem includes detailed HO_x- NO_x-BrOx-VOC-O_3 tropospheric chemistry (Bey et al., 2001; Mao et al., 2013; Marais et al., 2016; Parrella et al., 2012; Sherwen et al., 2016) of 250 chemical species and coupled stratospheric-tropospheric chemistry (Eastham et al., 2014), with emissions provided by the Harmonized Emissions Component (HEMCO) (Keller et al., 2014). Anthropogenic emissions are from the HTAP (Janssens-Maenhout et al., 2015) and RETRO (Schultz et al., 2008) inventories with updated scaling factors (F. Liu et al., 2018; Oda et al., 2018; van der Gon et al., 2011). Biomass burning emissions are determined from the Quick Fire Emission Database (QFED) (Koster et al., 2015) using MODIS fire data. Biogenic emissions are determined using MEGAN v2.1 (Guenther et al., 2012). Additional emissions are included for lightning and soil NO_x (Hudman et al., 2012; Murray et al., 2012), volcanic SO_2 (Carn, 2019), sea salt aerosols, oceanic emissions of dimethyl sulfide, acetone, acetaldehyde, iodine and soil dust (Knowland, Keller, & Lucchesi, 2022). The 24-hour simulation which serves as the starting point for the next forecast is constrained by the assimilated meteorology from the GEOS Forward Processing for Instrument Teams (FP-IT) (Lucchesi, 2013), a near-real time model system that is comparable to MERRA-2 (Gelaro et al., 2017). GEOS-Chem stratospheric ozone is weakly nudged to ozone from the GEOS-FP, which is constrained by assimilated satellite ozone measurements (Wargan et al., 2015). GEOS-CF version 1.0 does not currently assimilate any other trace gas or aerosol observations.

To minimize large data volume transfers and archiving, the GMAO produces a smaller TEMPO-specific GEOS-CF product for use in the TEMPO processing pipeline (Knowland, Keller, & Lucchesi, 2022). Upon completion of each daily GEOS-CF forecast, the most recent GEOS-CF TEMPO forecasts are downloaded to the TEMPO Science Data Processing Center (SDPC). The GEOS-CF TEMPO file is limited in extent to longitudes 180°E to 0° and latitudes 0° to 90°N and contains the mixing ratio vertical profiles of selected trace gases detectable in the UV/visible (O_3, NO_2, HCHO, SO_2, H_2O, BrO, $C_2H_2O_2$, HNO_2, IO) and relevant meteorological variables (surface pressure, temperature profile, 2-m eastward and northward winds, tropopause pressure and boundary layer height).

If for any reason GEOS-CF forecasts become unavailable, the TEMPO processing pipeline defaults to using a GEOS-CF climatology provided by GMAO. The climatology consists of monthly averages of the same GEOS-CF trace gases and meteorological variables as those provided in the GEOS-CF TEMPO daily forecasts. These monthly averages were created using a long-term dataset of GEOS-CF hindcasts from January 2018 to May 2021 (meteorological fields) and from January 2020 to May 2021 (chemical fields). The atmospheric profiles and parameters used in the TEMPO processing are created by linearly interpolating between the two monthly climatologies nearest to the date of observation. The HCHO Level 2 file metadata will indicate whether a forecast (*apriori_source* = "GEOSCF:forecast") or climatology (*apriori_source* = "GEOSCF:climatology") is used for the atmospheric profiles.

The same 72-layer definition as the GEOS-CF model is used in TEMPO output variables with a vertical dimension. These vertical layers follow a hybrid sigma-pressure grid, with each pressure level at the boundary of a layer defined by a set of fixed Eta coefficients *eta_a* and *eta_b* which are a function of layer number. The bottom boundary of a layer *i* is defined as

$$p_i = eta\_a_i + p_s \cdot eta\_b_i \tag{12}$$

with the top of the layer defined as

$$p_{i+1} = eta\_a_{i+1} + p_s \cdot eta\_b_{i+1} \tag{13}$$

In combination with the surface pressure p_s, the Eta coefficients can be used to reconstruct the vertical pressure grid for each TEMPO observation. The Eta coefficients are provided in Level 2 TEMPO trace gas files as attributes of the surface pressure variable.

Figure 8 shows examples of HCHO vertical profiles simulated by GEOS-CF for "clean" and "polluted" ground pixels and Figure 10 shows an example of the partial column of the lowermost layer of the GEOS-CF simulation.

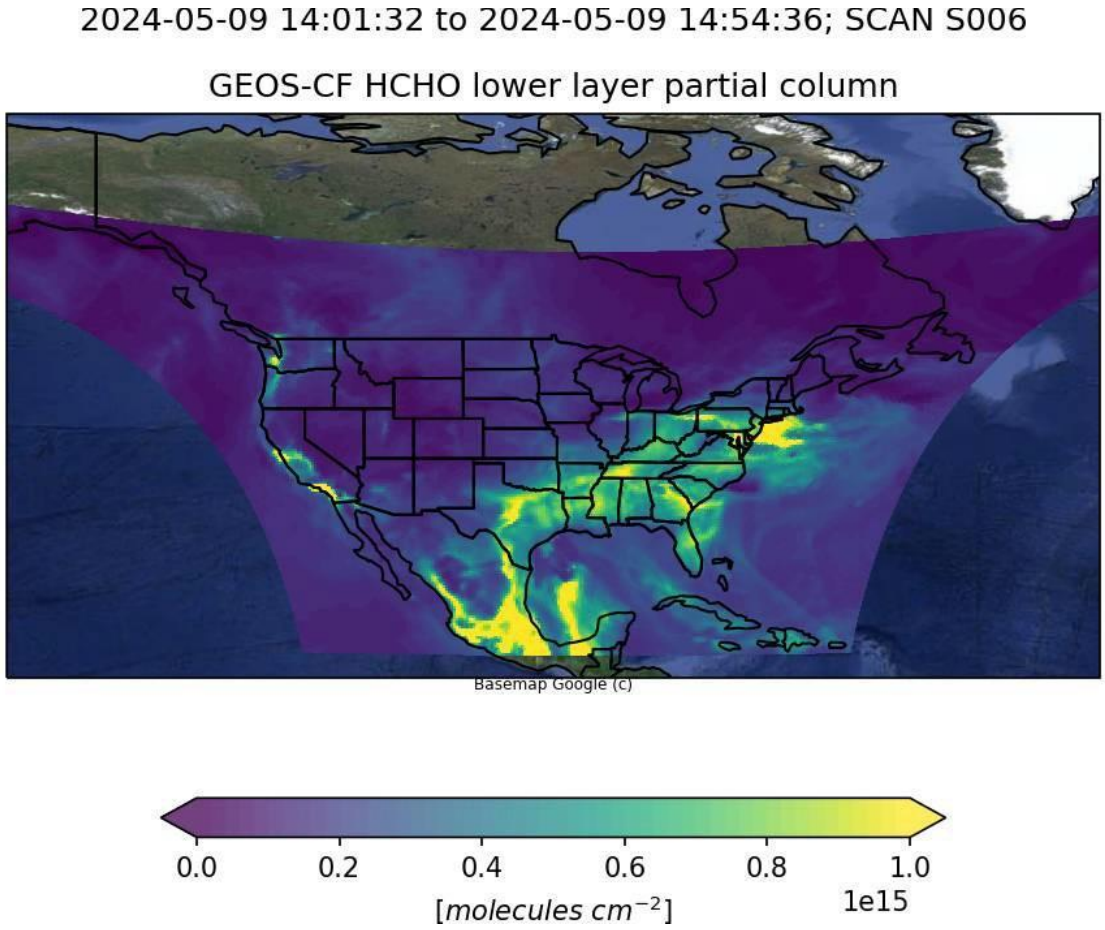

Figure 10. *Lower most layer, "surface", partial columns of HCHO simulated by the GEOS-CF forecasting system to support the calculation of TEMPO AMFs for scan #6, May 9, 2024.*

3.1.3.6 Terrain Pressure Correction

The use of an atmospheric model with coarser spatial resolution than the satellite

observations can lead to significant errors in the AMF in areas of inhomogeneous terrain elevation (Boersma et al., 2011; Zhou et al., 2009). In order to correct for terrain height inhomogeneities over the model grid cell, the surface pressure and atmospheric profiles are corrected using the effective terrain height for each satellite ground pixel as determined from the GMTED2010 high resolution digital elevation model (DEM) (Danielson & Gesch, 2011). This correction uses the hypsometric equation with linear temperature lapse rate (Zhou et al., 2009). The effective surface pressure $p_{s,obs}$ for each satellite observation is given by

$$p_{s,obs} = p_{s,model} \times \left[\frac{T_s}{T_s - \Gamma(h_{model} - h_{DEM})}\right]^{\frac{-g}{R\Gamma}} \quad (14)$$

where $p_{s,model}$ is the surface pressure from the coincident model grid cell, T_s is the corresponding surface temperature, h_{model} is the terrain altitude from the model, h_{DEM} is the effective terrain altitude derived from the DEM, $\Gamma = 6.5$ K m^{-1} is the temperature lapse rate, $R = 287$ J kg^{-1} K^{-1} is the gas constant of dry air, and $g = 9.81$ m s^{-2} is Earth's acceleration of gravity. Pressure levels for other layers are then adjusted using the Eta coefficients as described in the equations defining the pressure levels. While the surface and layer pressures and resulting air column change, trace gas mixing ratio profiles are conserved in each altitude layer.

3.1.3.7 Accounting for Aerosol Effects

Aerosols affect the light path of a photon through the atmosphere, and as a result, their presence in a scene will influence the altitude dependent scattering weights and the AMF. The effect of aerosols depends on their altitude and optical properties (Kwon et al., 2017; Leitão et al., 2010):

- Non-absorbing aerosols increase sensitivity to trace gas within and above the aerosol layer through an increase in scattering probability and photons returned from these altitudes. The sensitivity within a layer is also increased due to multiple scattering.
- Non-absorbing aerosols decrease sensitivity below the aerosol layer as they prevent photons from penetrating to lower altitudes.
- Absorbing aerosols decrease sensitivity below and within the aerosol layer by decreasing the total light path.

Aerosols are not currently considered explicitly in the AMF calculation, but the effect is implicitly accounted for through the use of TEMPO-retrieved cloud radiance fractions and cloud pressures. They are considered as a source of uncertainty in the final product.

3.1.4. Background Correction

As explained above, the use of a radiance reference requires the correction of the HCHO columns to account for the presence of HCHO spectral signatures in the radiance reference. The background correction (SCD_{bgr}) is calculated for each scan (all granules at once) considering the mean of the GEOS-CF slant columns (SCD_{model}) for pixels with cloud fractions smaller than 0.5, and subsequently applying a smoothing median filter in the North-South dimension. For each

cross track position the model slant columns are computed applying the AMF_i to the corresponding GEOS-CF vertical column ($VCD_{model,i}$):

$$\underline{SCD_{model}}(cross\ track) = \frac{\sum_i^n \quad VCD(cross\ track)_{model,i} \times AMF(cross\ track)_i}{n} \tag{15}$$

where n is the number of pixels with cloud fractions smaller than 0.5 in each cross track considered independently. The median filter uses a window of 250 cross track positions to determine the background correction:

$$SCD(cross\ track)_{bgr} = median_{k=250}\left[\underline{SCD(cross\ track)_{model}}\right] \tag{16}$$

where k is the size of the median filter window. For segments near both ends, mirror reflection (i.e., *dcba*|*abcd*|*dcba*) is applied to deal with the finite length. Figure 11 shows the background correction for the 9 granules of TEMPO scan number 6 on May 9, 2024.

The calculation of radiance references and background corrections should be consistent.

At the time of writing this ATBD, there are efforts to improve the current solution. This document will be updated in the future to reflect any changes. The net result of the current combination of radiance reference and background corrections, according to preliminary validation results, is a TEMPO HCHO low bias with respect to ground-based Fourier Transform Infrared Spectroscopy and TROPOMI observations, while it shows a better agreement with Pandora observations.

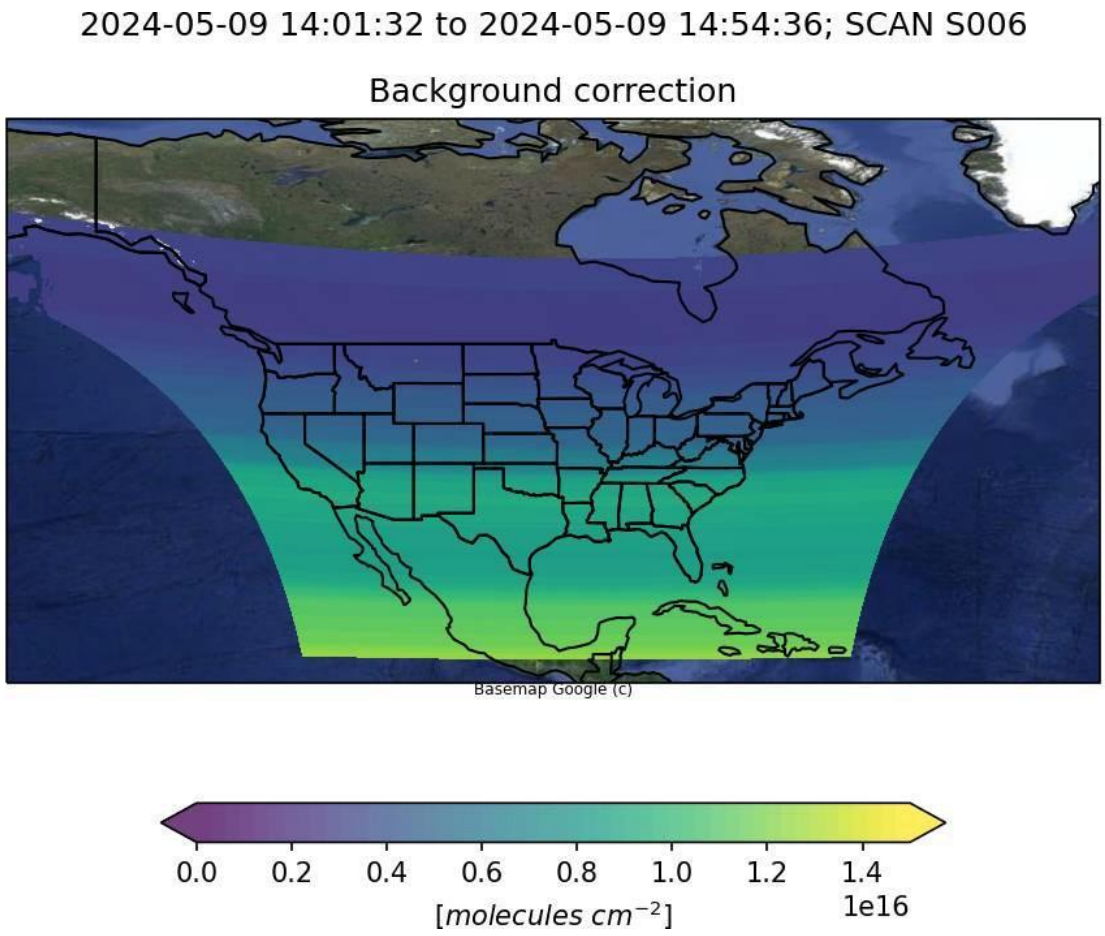

Figure 11. *TEMPO HCHO background correction for scan #6 on May 9, 2024.*

3.1.5. Scientific Theory Assumptions

Several assumptions are made in the derivation of version 3 HCHO vertical column densities:
1) Differential slant column density retrieval

- The atmospheric absorption of the trace gas is optically thin.
- The wavelength dependency of the surface reflectance, aerosol effects and instrument calibration issues can be approximated with low-order polynomials.

2) Air mass factor calculation

- Clouds are considered Lambertian surfaces with an albedo of 0.8.
- The independent pixel approximation is used, which considers each ground pixel to be composed of a clear-sky and cloud-sky part.
- The air mass factor is assumed to be constant through the fitting window and is calculated at 340 nm.
- All water bodies are treated as open ocean for the surface reflectance calculation, and shallow water/turbidity is not considered. The current algorithm treats ground pixel as

either land or water, and mixed surface types are not currently considered.

- Several assumptions are made in the use of the GLER for surface reflectance, including that the surface reflectance on a given day is accurately represented by a 22-year MODIS climatology which use kernels to approximate the BRDFs, and that GLER based on MODIS can be used at the more extreme viewing angles of geostationary orbit.
- The output of a priori trace gas profiles from the chemical transport model are considered as “truth”.
- Aerosols are considered implicitly through the use of retrieved cloud fraction and pressure.

3) Background correction

- The background corrections is assumed to be smoothly varying in the N/S direction.
- The output of a priori trace gas columns from the chemical transport model are considered as “truth”.

3.2. Algorithm Input Variables

Name	Long Name	Unit
product/cloud_fraction	effective cloud fraction from file TEMPO_CLDO4_L2	unitless
product/cloud_pressure	cloud pressure from file TEMPO_CLDO4_L2	hPa
band_290_490_nm/irradiance	irradiance from file TEMPO_IRR_L1	photons/s/cm^2/nm
band_290_490_nm/pixel_quality_flag	pixel quality flag from file TEMPO_IRR_L1	unitless
band_290_490_nm/sf_asym	slit function asymmetry parameter from file TEMPO_IRR_L1	unitless
band_290_490_nm/sf_hw1e	slit function half-width at 1/e parameter from file TEMPO_IRR_L1	nm
band_290_490_nm/sf_shape	wavelength calibration parameters from file TEMPO_IRR_L1	nm
band_290_490_nm/wavecal_params	wavelength calibration parameters from file TEMPO_IRR_L1	nm
band_290_490_nm/ground_pixel_quality_flag	ground pixel quality flag from file TEMPO_RAD_L1	unitless
band_290_490_nm/inr_quality_flag	INR quality flag from file TEMPO_RAD_L1	unitless
band_290_490_nm/latitude	latitude from file TEMPO_RAD_L1	degrees_north
band_290_490_nm/latitude_bounds	latitude bounds (NE,NW,SW,SE) from file TEMPO_RAD_L1	degrees_north
band_290_490_nm/longitude	longitude from file TEMPO_RAD_L1	degrees_east
band_290_490_nm/longitude_bounds	longitude bounds (NE,NW,SW,SE) from file TEMPO_RAD_L1	degrees_east
band_290_490_nm/pixel_quality_flag	pixel quality flag from file TEMPO_RAD_L1	unitless
band_290_490_nm/radiance	radiance from file TEMPO_RAD_L1	photons/s/cm^2/nm/sr
band_290_490_nm/snow_ice_fraction	snow ice fraction from file TEMPO_RAD_L1	unitless
band_290_490_nm/solar_azimuth_angle	solar azimuth angle from file	degrees

	TEMPO_RAD_L1	
band_290_490_nm/solar_zenith_angle	solar zenith angle from file TEMPO_RAD_L1	degrees
band_290_490_nm/terrain_height	area-weighted mean terrain height from file TEMPO_RAD_L1	m
band_290_490_nm/viewing_azimuth_angle	viewing azimuth angle from file TEMPO_RAD_L1	degrees
band_290_490_nm/viewing_zenith_angle	viewing zenith angle from file TEMPO_RAD_L1	degrees
band_290_490_nm/wavecal_params	wavelength calibration parameters from file TEMPO_RAD_L1	nm
earth_sun_distance	Earth-sun distance	m
mirror_step	scan mirror position index	unitless
time	exposure start time from file TEMPO_RAD_L1	seconds since 1980-01-06T00:00:00Z
HCHO	Formaldehyde (HCHO, MW =30.00 g mol^{-1}) volume mixing ratio dry air from GEOS-CF	mol mol^{-1}
O3	Ozone (O3, MW = 48.00 g mol^{-1}) volume mixing ratio dry air from file GEOS-CF	mol mol^{-1}
PHIS	surface geopotential height from file GEOS-CF	m^2/s^2
PS	surface pressure from file GEOS-CF	Pa
T	air temperature from file GEOS-CF	K
TROPPB	tropopause pressure based on blended estimate from file GEOS-CF	Pa
U2M	2-meter eastward wind from file GEOS-CF	m/s
V2M	2-meter northward wind from file GEOS-CF	m/s
lat	latitude from file GEOS-CF	degrees_north
lon	longitude from file GEOS-CF	degrees_east
Ap	Eta_a coefficients from GEOS-Chem_72_layer_vertical_grid.nc	hPa
Bp	Eta_b coefficients from GEOS-Chem_72_layer_vertical_grid.	unitless

	nc	
alb	albedo from GLER land/snow/ocean files	unitless
doy	day of year from GLER land/snow/ocean files	No content available.
hour	hour from GLER land/snow/ocean files	hour
lat	latitude from GLER land/snow/ocean files	degrees_north
lon	longitude from GLER land/snow/ocean files	degrees_east
qf	quality flag from GLER land/snow/ocean files	unitless
Grid/Albedo	albedo from AMF LUT file	unitless
Grid/OZO	ozone profile from AMF LUT file	string
Grid/Surface_Pressure	surface pressure from AMF LUT file	hPa
Grid/SZA	solar zenith angle from AMF LUT file	degrees
Grid/VZA	viewing zenith angle from AMF LUT file	degrees
Grid/Wavelength	wavelength from AMF LUT file	nm
Intensity/I0	radiance I0 from AMF LUT file	W/cm^2
Intensity/I1	radiance I1 from AMF LUT file	W/cm^2
Intensity/I2	radiance I2 from AMF LUT file	W/cm^2
Intensity/Ir	radiance Ir from AMF LUT file	W/cm^2
Intensity/Sb	multiple surface reflection term from AMF LUT file	unitless
Profiles/Air_Column_Layer	air column layer from AMF LUT file	W/cm^2
Profiles/Altitude_Layer	altitude layer from AMF LUT file	km
Profiles/Altitude_Level	altitude level from AMF LUT file	km
Profiles/Ozone_Column_Layer	ozone column layer from AMF LUT file	$molecules/cm^2$
Profiles/Pressure_Layer	pressure layer from AMF LUT	hPa

	file	
Profiles/Pressure_Level	pressure layer from AMF LUT file	hPa
Profiles/Temperature_Level	temperature level from AMF LUT file	K
Scattering_Weights/dI0	scattering weights from AMF LUT file	unitless
Scattering_Weights/dI1	scattering weights from AMF LUT file	unitless
Scattering_Weights/dI2	scattering weights from AMF LUT file	unitless

3.3. Algorithm Output Variables

Name	Long Name	Unit
geolocation/latitude	pixel center latitude	degrees_north
geolocation/latitude_bounds	pixel corner latitude	degrees_north
geolocation/longitude	pixel center longitude	degrees_east
geolocation/longitude_bounds	pixel corner longitude	degrees_east
geolocation/relative_azimuth_angle	relative azimuth angle at pixel center	degrees
geolocation/solar_azimuth_angle	solar azimuth angle at pixel center	degrees
geolocation/solar_zenith_angle	solar zenith angle at pixel center	degrees
geolocation/time	radiance exposure start time	seconds since 1980-01-06T00:00:00Z
geolocation/viewing_azimuth_angle	viewing azimuth angle at pixel center	degrees
geolocation/viewing_zenith_angle	viewing zenith angles	degrees
mirror_step	scan mirror position index	unitless
product/main_data_quality_flag	main data quality flag	unitless
product/vertical_column	formaldehyde vertical column	molecules/cm^2
product/vertical_column_uncertainty	formaldehyde vertical column uncertainty	molecules/cm^2
qa_statistics/fit_convergence_flag	radiance fit convergence flag	unitless
qa_statistics/fit_rms_residual	radiance fit RMS residual	unitless
support_data/albedo	surface albedo	unitless
support_data/amf	formaldehyde air mass factor	unitless
support_data/amf_cloud_fraction	cloud fraction	unitless
support_data/amf_cloud_pressure	cloud pressure	hPa
support_data/amf_diagnostic_flag	formaldehyde air mass factor diagnostic flag	unitless
support_data/background_correction	background correction	molecules/cm^2
support_data/eff_cloud_fraction	effective cloud fraction	unitless
support_data/fitted_slant_column	formaldehyde fitted slant column	molecules/cm^2
support_data/fitted_slant_column_uncertainty	formaldehyde fitted slant column uncertainty	molecules/cm^2
support_data/gas_profile	vertical profile of	molecules/cm^2

	formaldehyde partial column	
support_data/ground_pixel_quality_flag	ground pixel quality flag	unitless
support_data/scattering_weights	vertical profile of scattering weights	unitless
support_data/snow_ice_fraction	fraction of pixel area covered by snow and/or ice	unitless
support_data/surface_pressure	surface pressure	hPa
support_data/temperature_profile	air temperature	K
support_data/terrain_height	terrain height	m
xtrack	pixel index along slit	unitless

4. Algorithm Usage Constraints

Users of the trace gas products should at minimum apply filtering of the data considering the main data quality flag and cloud fraction. For the majority of users of version 3 HCHO, we recommend to use only data where *main_data_quality_flag* = 0 and *eff_cloud_fraction* < 0.2. Note that Level 3 products (gridded data for the entire scan) are not pre-filtered, and the same filtering recommendations apply to Level 3.

The *main_data_quality_flag* variable in the product group of the Level 2 and Level 3 files provides a high-level approximation to product quality. Table 8 provides the definition of the *main_data_quality_flag* for HCHO retrievals. More information on data usage, known issues and file structure may be found in the TEMPO Trace Gas and Cloud Level 2 and 3 Data Products User Guide (Gonzalez Abad et al., 2024) Note that Level 3 products (gridded data for the entire scan) are not pre-filtered, and the same filtering recommendations apply to Level 3 as to Level 2.

Table 8. *Logic employed to set the values of the main_data_quality_flag for version 3 TEMPO data. The variable fit_convergence_flag is provided in the qa_statistics group of the Level 2 files. VCD values are provided in the product group of the Level 2 files. The values of dSCD, $dSCD_{uncert}$, amf_diagnostic_flag and AMF are provided in the support_data group of the Level 2 files. The geometric air mass factor AMF_{geo} is calculated as (sec(SZA) + sec(VZA)).*

Value	Meaning	Description	
0	Normal	fit_convergence_flag = 1	AND
		(-5e^{17} molecules cm^{-2}) <= VCD <= 5e^{17} molecules cm^{-2})	AND
		((dSCD + 2*$dSCD_{uncert}$) >= 0)	AND
		AMF_{geo} <= 6	AND
		AMF >= 0.1	
1	Suspicious	fit_convergence_flag = 0	OR
		(((dSCD + 2*$dSCD_{uncert}$) < 0) AND	
		((dSCD + 3*$dSCD_{uncert}$) >= 0))	OR
		(VCD < -5e^{17} molecules cm^{-2})	OR
		(VCD > -5e^{17} molecules cm^{-2})	OR
		AMF_{geo} > 6	OR
		AMF < 0.1	
2	Bad	fit_convergence_flag < 0	OR
		((dSCD + 3*$dSCD_{uncert}$) < 0)	OR
		amf_diagnostic_flag(bit1) = 1	

Retrievals of the highest quality have a *main_data_quality_flag* equal to “0”. This flag

considers the value of the VCDs to detect outliers, the viewing geometry for each pixel and the availability of a successful AMF calculation. Owing to increased uncertainties in the spectral fitting and AMF calculations, pixels with geometric AMF (AMF_{geo}) larger than 6 (SZA > ~70° and VZA > ~70°) are categorized as "suspect" with *main_data_quality_flag* equal to "1". Pixels categorized as "suspect" may carry useful information, but their interpretation requires further analysis. Fitting uncertainties in early and late hours of the day increase, and the sensitivity of TEMPO to lower tropospheric HCHO is reduced. Those pixels identified as outliers or without a successful AMF calculation are categorized as bad with a *main_data_quality_flag* value equal to "2".

TEMPO HCHO measurements should also be filtered by cloud fraction for several reasons. First, clouds obscure the lower atmosphere, leading to less sensitivity to the column near the surface and larger uncertainties, even for high quality radiance observations. In addition, version 3 HCHO spectral fitting is known to degrade over partly cloudy pixels due to the inhomogeneous illumination of the instrument slit, resulting in large fitting uncertainties in the retrieved SCD in these partly cloudy scenes. Finally, the version 3 cloud fraction product is known to have a high bias due to a Level 1B overestimation of the absolute radiance (González Abad et al., 2024). In consequence, the recommendation is to use only the highest quality retrievals by limiting analyses to pixels with effective cloud fractions (*support_data/eff_cloud_fraction*) < 0.2. More strict cloud fraction criterion (e.g., < 0.15) will retain less data, though the retained data will have less cloud influence. Users are thus advised to adjust based on their tolerance. This cloud fraction recommendation is for the current data version, and the cloud filter recommendation may change for future data releases.

GLER look-up-table accuracy is difficult to assess, particularly over snow and ice, bright surfaces, and quality of the MODIS product for TEMPO geometries. Thus, we recommend using the *snow_ice_fraction* in the *support_data* group to identify pixels covered by snow and ice and treat them with care.

The *geolocation* and *support_data* groups contain variables necessary to interpret the observations. The *support_data*/*amf_diagnostic_flag* is a 16-bit bitwise flag indicating different assumptions/issues in the air mass factor calculation, which advanced users may wish to consult for further insight. The following table provides the meaning of each bit in the *amf_diagnostic_flag*.

Table 9. *Meaning of each bit of amf_diagnostic_flag in Level 2 HCHO files*

Bit	**Bit Meaning**
bit0	Good AMF
bit1	Bad AMF / no AMF calculation performed
bit2	Warning: pixel affected by glint
bit3	Warning: climatological cloud pressure information used
bit4	Warning: adjusted surface pressure (original surface pressure outside LUT bounds)

bit5	Warning: adjusted cloud pressure (original cloud pressure outside LUT bounds)
bit6	Not used / reserved for future use
bit7	Not used / reserved for future use
bit8	Not used / reserved for future use
bit9	Not used / reserved for future use
bit10	Error: no albedo information
bit11	Error: no cloud information
bit12	Error: no trace gas profile information
bit13	Error: no scattering weight calculation
bit14	Error: no geolocation information available
bit15	Not used / reserved for future use

5. Performance Assessment

5.1. Validation Methods

The TEMPO HCHO validation plan and methods are described in the Level 2 Science Data Product Validation Plan document (TEMPO Validation Team, 2023). The validation plan outlines a validation approach to meet the Program Level Requirements Appendix (PLRA) baseline requirement for TEMPO HCHO validation and to extend the validation in a best effort approach to leverage measurement and modeling assets over the TEMPO baseline mission. This includes the use of ground-based and satellite observations for routine validation, as well as episodic field missions.

The TEMPO validation plan defines three levels of product maturity:

1. **Beta**: Product is minimally validated but may contain significant errors. Publications using these data are discouraged.
2. **Provisional**: Product performance has been demonstrated through a large, but still (seasonally or otherwise) limited number of independent measurements. The product is potentially ready for operational users and may be suitable for scientific publication.
3. **Full**: Product performance has been demonstrated over a large and wide range of representative conditions, with comprehensive documentation of product performance, including known anomalies and their remediation strategies. Products are ready for systematic use and suitable for scientific application and publication.

Correlative datasets that may be used for routine assessment of TEMPO HCHO are included in the following table:

Table 10. *Datasets for routine assessment of TEMPO HCHO*

Dataset	Description	Website
NDACC	Network of direct Sun FTIR spectrometers	https://ndacc.larc.nasa.gov/
PGN	Network of Pandora spectrometers (total column and MAX-DOAS geometry)	https://www.pandonia-global-network.org/
S5P_L2__HCHO___HiR	HCHO retrievals from Sentinel-5P TROPOMI satellite instrument	https://disc.gsfc.nasa.gov/datasets/S5P_L2__HCHO___HiR_2/summary

In addition to these datasets, TEMPO HCHO has been intercompared with HCHO from the LEO satellite instruments TROPOMI, OMI and OMPS. Multiple field campaigns that

include airborne in situ and remote sensing instruments are conducted during the TEMPO baseline mission, providing valuable data for HCHO validation. These campaigns include Synergistic TEMPO Air Quality Science (STAQS), Atmospheric Emissions and Reactions Observed from Megacities to Marine Areas (AEROMMA), Coastal Urban Plume Dynamics Study (CUPiDS), and Northeast Corridor Air Quality and Greenhouse Gas (NEC-AQ-GHG) Study. These campaigns occurred during Summer 2023, overlapping with the first month of TEMPO operations; additional campaigns with TEMPO validation components are anticipated for future years including summer Student Airborne Research Program (SARP) flights and the Hemispheric Airborne Measurements of Air Quality (HAMAQ) anticipated in Summer 2028.

The TEMPO validation team carried out a series of comprehensive validation studies during the first year of TEMPO operations. Based on the results of these studies, the HCHO version 3 product has been declared at provisional maturity level. Users should refer to the TEMPO validation report (TEMPO Validation Team, 2025) for detailed validation results.

5.2. Uncertainties

Due to their ability to measure the HCHO column with high temporal frequency, FTIR and Pandora instruments in the NDACC and PGN networks are the backbone of TEMPO HCHO validation. Models, such as WRF-Chem and CMAQ, may also be used as comparison platforms for non-coincident validation measurements. Uncertainties of the correlative datasets vary. Details of these uncertainties are included in the Validation Plan or in individual dataset references.

5.3. Validation Errors

HCHO column uncertainties from spectral fitting are provided in the Level 2 product.

Previous experience with OMI and OMPS instruments shows random fitting uncertainties in the 45% to 100% range for hotspot and background concentrations respectively (González Abad et al., 2015; Nowlan et al., 2023). TEMPO has better SNR than OMI, OMPS and TROPOMI in the HCHO fitting region, leading to smaller random uncertainty. Figure 12 shows the distribution of TEMPO VCD fitting uncertainties for scan #6 on May 9, 2024. The red vertical line indicates the mission requirement precision for 12 co-added observations. TEMPO HCHO far exceeds the mission precision requirement, with more than 90% of TEMPO single observations having less uncertainty than the required precision of 12 co-added pixels. In the version 3 retrievals, the precision of the retrievals degrades in the presence of partial or inhomogeneous clouds due to inhomogeneous illumination of the instrument slit for these scenes.

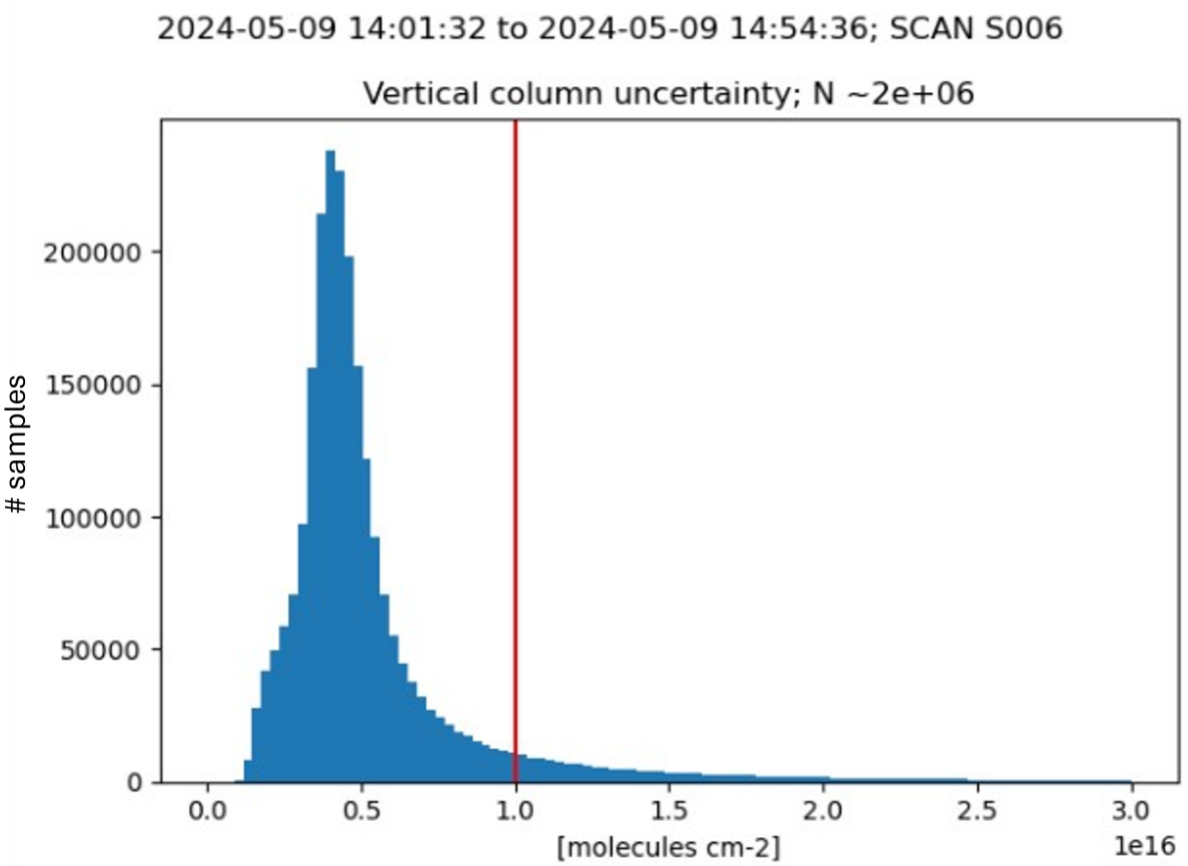

Figure 12. *Histogram of TEMPO HCHO vertical column uncertainty (precision) included in the Level 2 files for scan #6 on May 9, 2024. The vertical red line marks the TEMPO mission requirement for a precision of 1x10^{16} molecules cm^{-2} for 12 co-added ground pixels.*

Systematic errors in the slant columns can result from model parameter errors and instrumental effects. (De Smedt et al., 2018) estimate the systematic uncertainty of HCHO slant columns to be around 20%. (Lorente et al., 2017) performed a detailed study comparing multiple OMI HCHO retrieval results from different algorithm groups. They estimated a structural uncertainty in the HCHO AMF due to the use of different ancillary data and cloud and aerosols estimates to be on average 42% over polluted regions and 31% over unpolluted regions. The most significant impacts were from trace gas profiles, surface albedo and clouds. This is in good agreement with uncertainties between 35% to 50% reported in the literature for HCHO AMF calculations (González Abad et al., 2015, 2016). TEMPO HCHO AMF calculations do not consider aerosols explicitly resulting in errors around ~20% with typical aerosol loadings but can become much larger in situations with high loadings, for example in wildfire smoke plumes (Jung et al., 2019). Aerosols are implicitly considered to some extent through the cloud fractions derived by TEMPO's cloud product algorithm, however, the influence of different types of aerosols on TEMPO cloud retrieval (and therefore trace gas AMFs) still awaits further study. The performance of TEMPO AMF calculations at high solar zenith angles (above 70°) still needs to be assessed after addressing uncertainties associated with GLER LUTs, and non-spherical

scattering weights. Nonetheless, Figure 13, showing the dependency of the fitting uncertainty with solar zenith angle, suggests that TEMPO dSCDs at least may be useful beyond 70° (see *main_data_quality_flag* logic table).

The current version 3 TEMPO retrievals have a high bias in the retrieved effective cloud fraction determined in the cloud algorithm (Wang et al., 2025), which will propagate errors to the final trace gas products in clear (cloud-free) skies. This is likely caused by a combination of high bias in version 3 L1B calibrated radiances and biases in the GLER over land. Biases in the GLER will also affect the trace gas retrievals directly by introducing errors in the calculation of the scattering weights. In most cases, the high bias in cloud fraction will result in a high bias in the retrieved HCHO column in polluted areas.

The quantification of on-orbit precision and accuracy from validation activities is an ongoing effort led by TEMPO's validation team. Please refer to TEMPO validation reports for a detailed analysis of TEMPO HCHO performance.

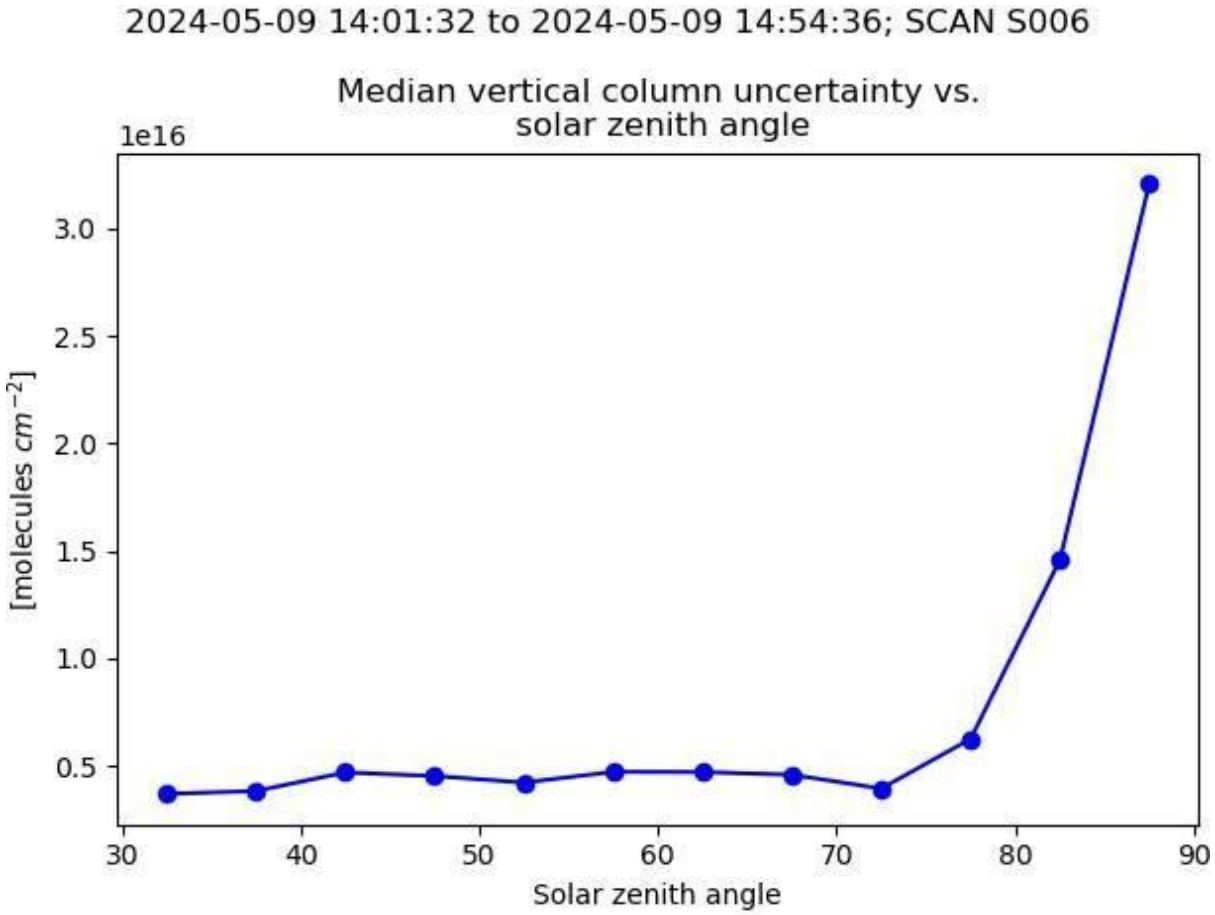

Figure 13. *TEMPO HCHO vertical column uncertainty as a function of solar zenith angle for retrievals performed using scan #6 on May 9, 2024.*

6. Algorithm Implementation

6.1. Algorithm Availability

The TEMPO HCHO algorithm has been integrated in the TEMPO Science Data Processing Center (SDPC) pipeline at the Smithsonian Astrophysical Observatory. SDPC v4.4 is used to produce the data publicly released in May 2024 (version 3).

6.2. Input Data Data Access

URL	Description
https://dx.doi.org/10.5067/IS-40e/TEMPO/IRR_L1.003	TEMPO Level 1B Irradiance Product
https://dx.doi.org/10.5067/IS-40e/TEMPO/RAD_L1.003	TEMPO Level 1B Radiance Product
https://dx.doi.org/10.5067/IS-40e/TEMPO/CLDO4_L2.003	TEMPO Level 2 Cloud Product

6.3. Output Data Data Access

URL	Description
https://dx.doi.org/10.5067/IS-40e/TEMPO/HCHO_L2.003	TEMPO Level 2 HCHO Product
https://dx.doi.org/10.5067/IS-40e/TEMPO/HCHO_L3.003	TEMPO Level 3 (gridded) HCHO Product

6.4. Important Related URLs

URL	Description
https://tempo.si.edu	SI project homepage
https://asdc.larc.nasa.gov/project/TEMPO	ASDC project homepage

Contact Details

Gonzalo González Abad	
Roles	Writing – original draft, Writing – review & editing & Corresponding Author
Affiliations	Center for Astrophysics | Harvard & Smithsonian
Email	ggonzalezabad@cfa.harvard.edu
URL	https://www.cfa.harvard.edu/people/gonzalo-gonzalez-abad
UUID	https://orcid.org/0000-0002-8090-6480

Xiong Liu	
Roles	Writing – original draft, Writing – review & editing & Funding acquisition
Affiliations	Center for Astrophysics | Harvard & Smithsonian
Email	xliu@cfa.harvard.edu
URL	https://lweb.cfa.harvard.edu/~xliu/
UUID	http://orcid.org/0000-0003-2939-574X

Caroline Nowlan	
Roles	Writing – original draft & Writing – review & editing
Affiliations	Center for Astrophysics | Harvard & Smithsonian
Email	cnowlan@cfa.harvard.edu
URL	https://www.cfa.harvard.edu/people/caroline-nowlan
UUID	https://orcid.org/0000-0002-8718-9752

Huiqun Wang	
Roles	Writing – review & editing
Affiliations	Center for Astrophysics | Harvard & Smithsonian
Email	hwang@cfa.harvard.edu
URL	https://lweb.cfa.harvard.edu/~hwang/
UUID	https://orcid.org/0000-0001-9722-9992

References

Aliwell, S. R., Van Roozendael, M., Johnston, P. V., Richter, A., Wagner, T., Arlander, D. W., Burrows, J. P., Fish, D. J., Jones, R. L., Tørnkvist, K. K., Lambert, J.-C., Pfeilsticker, K., & Pundt, I. (2002). Analysis for BrO in zenith-sky spectra: An intercomparison exercise for analysis improvement. *Journal of Geophysical Research: Atmospheres*, *107*(D14), ACH 10-1-ACH 10-20. https://doi.org/10.1029/2001JD000329

Alvarado, L. M. A., Richter, A., Vrekoussis, M., Hilboll, A., Kalisz Hedegaard, A. B., Schneising, O., & Burrows, J. P. (2020). Unexpected long-range transport of glyoxal and formaldehyde observed from the Copernicus Sentinel-5 Precursor satellite during the 2018 Canadian wildfires. *Atmospheric Chemistry and Physics*, *20*(4), 2057–2072. https://doi.org/10.5194/acp-20-2057-2020

Bak, J., Liu, X., Kim, J.-H., Haffner, D. P., Chance, K., Yang, K., & Sun, K. (2017). Characterization and correction of OMPS nadir mapper measurements for ozone profile retrievals. *Atmos. Meas. Tech.*, *10*(11), 4373–4388. https://doi.org/10.5194/amt-10-4373-2017

Barkley, M. P., González Abad, G., Kurosu, T. P., Spurr, R., Torbatian, S., & Lerot, C. (2017). OMI air-quality monitoring over the Middle East. *Atmospheric Chemistry and Physics*, *17*(7), 4687–4709. https://doi.org/10.5194/acp-17-4687-2017

Barkley, M. P., Smedt, I. D., Van Roozendael, M., Kurosu, T. P., Chance, K., Arneth, A., Hagberg, D., Guenther, A., Paulot, F., Marais, E., & Mao, J. (2013). Top-down isoprene emissions over tropical South America inferred from SCIAMACHY and OMI formaldehyde columns. *Journal of Geophysical Research: Atmospheres*, *118*(12), 6849–6868. https://doi.org/10.1002/jgrd.50552

Bauwens, M., Stavrakou, T., Müller, J.-F., Smedt, I. D., Roozendael, M. V., Werf, G. R. van der, Wiedinmyer, C., Kaiser, J. W., Sindelarova, K., & Guenther, A. (2016). Nine years of global hydrocarbon emissions based on source inversion of OMI formaldehyde observations. *Atmospheric Chemistry and Physics*, *16*(15), 10133–10158. https://doi.org/10.5194/acp-16-10133-2016

Beirle, S., Lampel, J., Lerot, C., Sihler, H., & Wagner, T. (2017). Parameterizing the instrumental spectral response function and its changes by a super-Gaussian and its derivatives. *Atmospheric Measurement Techniques*, *10*(2), 581–598. https://doi.org/10.5194/amt-10-581-2017

Bey, I., Jacob, D. J., Yantosca, R. M., Logan, J. A., Field, B. D., Fiore, A. M., Li, Q., Liu, H. Y., Mickley, L. J., & Schultz, M. G. (2001). Global modeling of tropospheric chemistry with assimilated meteorology: Model description and evaluation. *Journal of Geophysical Research: Atmospheres*, *106*(D19), 23073–23095. 85.6. https://doi.org/10.1029/2001JD000807

Boersma, K. F., Eskes, H. J., Dirksen, R. J., der A, R. J. van, Veefkind, J. P., Stammes, P., Huijnen, V., Kleipool, Q. L., Sneep, M., Claas, J., Leitão, J., Richter, A., Zhou, Y., & Brunner, D. (2011). An improved tropospheric NO_2 column retrieval algorithm for the Ozone Monitoring Instrument. *Atmospheric Measurement Techniques*, *4*(9), 1905–1928. https://doi.org/10.5194/amt-4-1905-2011

Calvert, J. G., Orlando, J. J., Stockwell, W. R., & Wallington, T. J. (2015). *The Mechanisms of Reactions Influencing Atmospheric Ozone*. Oxford University Press.

Carn, S. (2019). *GES DISC Dataset: Multi-Satellite Volcanic Sulfur Dioxide L4 Long-Term Global Database V3, Greenbelt, MD, USA, Goddard Earth Science Data and Information Services Center (GES DISC)*. https://disc.gsfc.nasa.gov/datasets/MSVOLSO2L4_4/summary

Chan Miller, C., Gonzalez Abad, G., Wang, H., Liu, X., Kurosu, T., Jacob, D. J., & Chance, K. (2014). Glyoxal retrieval from the Ozone Monitoring Instrument. *Atmos. Meas. Tech.*, *7*(11), 3891–3907. https://doi.org/10.5194/amt-7-3891-2014

Chan Miller, C., Jacob, D. J., Marais, E. A., Yu, K., Travis, K. R., Kim, P. S., Fisher, J. A., Zhu, L., Wolfe, G. M., Hanisco, T. F., Keutsch, F. N., Kaiser, J., Min, K.-E., Brown, S. S., Washenfelder, R. A., González Abad, G., & Chance, K. (2017). Glyoxal yield from isoprene oxidation and relation to formaldehyde: Chemical mechanism, constraints from SENEX aircraft observations,

and interpretation of OMI satellite data. *Atmos. Chem. Phys.*, *17*(14), 8725–8738. https://doi.org/10.5194/acp-17-8725-2017

Chan Miller, C., Nowlan, C. R., Bak, J., Liu, X., Gonzalez Abad, G., Zoogman, P., & Chance, K. (2019). *A probabilistic model of surface reflectance for atmospheric retrieval algorithms from the UV to SWIR. 2019*, A13J-2935. AGU Fall Meeting Abstracts.

Chance, K., Kurosu, T. P., & Sioris, C. E. (2005). Undersampling correction for array detector-based satellite spectrometers. *Applied Optics*, *44*(7), 1296–1304. https://doi.org/10.1364/AO.44.001296

Chance, K., & Orphal, J. (2011). Revised ultraviolet absorption cross sections of H2CO for the HITRAN database. *Journal of Quantitative Spectroscopy and Radiative Transfer*, *112*(9), 1509–1510. https://doi.org/10.1016/j.jqsrt.2011.02.002

Chance, K., Palmer, P. I., Spurr, R. J. D., Martin, R. V., Kurosu, T. P., & Jacob, D. J. (2000). Satellite observations of formaldehyde over North America from GOME. *Geophysical Research Letters*, *27*(21), 3461–3464. https://doi.org/10.1029/2000GL011857

Chance, K. V., & Spurr, R. J. D. (1997). Ring effect studies: Rayleigh scattering, including molecular parameters for rotational Raman scattering, and the Fraunhofer spectrum. *Applied Optics*, *36*(21), 5224–5230. https://doi.org/10.1364/AO.36.005224

Chong, H., Houck, J., Flittner, D., James, C., Hou, W., Liu, X., & David, J. (2025). *Algorithm theoretical basis document for the TEMPO Level 0-1 processor*. TBD

Coddington, O. M., Richard, E. C., Harber, D., Pilewskie, P., Woods, T. N., Snow, M., Chance, K., Liu, X., & Sun, K. (2023). Version 2 of the TSIS-1 Hybrid Solar Reference Spectrum and Extension to the Full Spectrum. *Earth and Space Science*, *10*(3), e2022EA002637. https://doi.org/10.1029/2022EA002637

Cox, C., & Munk, W. (1954). Measurement of the Roughness of the Sea Surface from Photographs of the Sun's Glitter. *JOSA*, *44*(11), 838–850. https://doi.org/10.1364/JOSA.44.000838

Danielson, J. J., & Gesch, D. B. (2011). Global multi-resolution terrain elevation data 2010 (GMTED2010). In *Open-File Report* (Nos. 2011–1073). U.S. Geological Survey. https://doi.org/10.3133/ofr20111073

De Smedt, I., Müller, J.-F., Stavrakou, T., van der A, R., Eskes, H., & Van Roozendael, M. (2008). Twelve years of global observations of formaldehyde in the troposphere using GOME and SCIAMACHY sensors. *Atmos. Chem. Phys.*, *8*(16), 4947–4963. https://doi.org/10.5194/acp-8-4947-2008

De Smedt, I., Roozendael, M. V., Stavrakou, T., Müller, J.-F., Lerot, C., Theys, N., Valks, P., Hao, N., & der A, R. van. (2012). Improved retrieval of global tropospheric formaldehyde columns from GOME-2/MetOp-A addressing noise reduction and instrumental degradation issues. *Atmospheric Measurement Techniques*, *5*(11), 2933–2949. https://doi.org/10.5194/amt-5-2933-2012

De Smedt, I., Stavrakou, T., Hendrick, F., Danckaert, T., Vlemmix, T., Pinardi, G., Theys, N., Lerot, C., Gielen, C., Vigouroux, C., Hermans, C., Fayt, C., Veefkind, P., Müller, J.-F., & Van Roozendael, M. (2015). Diurnal, seasonal and long-term variations of global formaldehyde columns inferred from combined OMI and GOME-2 observations. *Atmospheric Chemistry and Physics*, *15*(21), 12519–12545. https://doi.org/10.5194/acp-15-12519-2015

De Smedt, I., Theys, N., Yu, H., Danckaert, T., Lerot, C., Compernolle, S., Roozendael, M. V., Richter, A., Hilboll, A., Peters, E., Pedergnana, M., Loyola, D., Beirle, S., Wagner, T., Eskes, H., Geffen, J. van, Boersma, K. F., & Veefkind, P. (2018). Algorithm theoretical baseline for formaldehyde retrievals from S5P TROPOMI and from the QA4ECV project. *Atmospheric Measurement Techniques*, *11*(4), 2395–2426. https://doi.org/10.5194/amt-11-2395-2018

Duncan, B. N., Prados, A. I., Lamsal, L. N., Liu, Y., Streets, D. G., Gupta, P., Hilsenrath, E., Kahn, R. A., Nielsen, J. E., Beyersdorf, A. J., Burton, S. P., Fiore, A. M., Fishman, J., Henze, D. K., Hostetler, C. A., Krotkov, N. A., Lee, P., Lin, M., Pawson, S., … Ziemba, L. D. (2014). Satellite data of atmospheric pollution for U.S. air quality applications: Examples of applications, summary of data end-user resources, answers to FAQs, and common mistakes to avoid. *Atmospheric Environment*, *94*, 647–662. https://doi.org/10.1016/j.atmosenv.2014.05.061

Eastham, S. D., Weisenstein, D. K., & Barrett, S. R. H. (2014). Development and evaluation of the unified tropospheric–stratospheric chemistry extension (UCX) for the global chemistry-transport model GEOS-Chem. *Atmospheric Environment*, *89*, 52–63. https://doi.org/10.1016/j.atmosenv.2014.02.001

Fasnacht, Z., Vasilkov, A., Haffner, D., Qin, W., Joiner, J., Krotkov, N., Sayer, A. M., & Spurr, R. (2019). A geometry-dependent surface Lambertian-equivalent reflectivity product for UV–Vis retrievals – Part 2: Evaluation over open ocean. *Atmospheric Measurement Techniques*, *12*(12), 6749–6769. https://doi.org/10.5194/amt-12-6749-2019

Finkenzeller, H., & Volkamer, R. (2022). O2–O2 CIA in the gas phase: Cross-section of weak bands, and continuum absorption between 297–500 nm. *Journal of Quantitative Spectroscopy and Radiative Transfer*, *279*, 108063. https://doi.org/10.1016/j.jqsrt.2021.108063

Fishman, J., Iraci, L. T., Al-Saadi, J., Chance, K., Chavez, F., Chin, M., Coble, P., Davis, C., DiGiacomo, P. M., Edwards, D., Eldering, A., Goes, J., Herman, J., Hu, C., Jacob, D. J., Jordan, C., Kawa, S. R., Key, R., Liu, X., … Wang, M. (2012). *The United States' Next Generation of Atmospheric Composition and Coastal Ecosystem Measurements: NASA's Geostationary Coastal and Air Pollution Events (GEO-CAPE) Mission*. https://doi.org/10.1175/BAMS-D-11-00201.1

Flynn, L., Long, C., Wu, X., Evans, R., Beck, C. T., Petropavlovskikh, I., McConville, G., Yu, W., Zhang, Z., Niu, J., Beach, E., Hao, Y., Pan, C., Sen, B., Novicki, M., Zhou, S., & Seftor, C. (2014). Performance of the Ozone Mapping and Profiler Suite (OMPS) products. *Journal of Geophysical Research: Atmospheres*, *119*(10), 6181–6195. https://doi.org/10.1002/2013JD020467

Gelaro, R., McCarty, W., Suárez, M. J., Todling, R., Molod, A., Takacs, L., Randles, C. A., Darmenov, A., Bosilovich, M. G., Reichle, R., Wargan, K., Coy, L., Cullather, R., Draper, C., Akella, S., Buchard, V., Conaty, A., da Silva, A. M., Gu, W., … Zhao, B. (2017). The Modern-Era Retrospective Analysis for Research and Applications, Version 2 (MERRA-2). *Journal of Climate*, *30*(14), 5419–5454. https://doi.org/10.1175/JCLI-D-16-0758.1

González Abad, G., Liu, X., Chance, K., Wang, H., Kurosu, T. P., & Suleiman, R. (2015). Updated Smithsonian Astrophysical Observatory Ozone Monitoring Instrument (SAO OMI) formaldehyde retrieval. *Atmospheric Measurement Techniques*, *8*(1), 19–32. https://doi.org/10.5194/amt-8-19-2015

González Abad, G., Nowlan, C., Wang, H., Chong, H., Houck, J., Liu, X., & Chance, K. (2024). *TEMPO Trace Gas and Cloud Level 2 and 3 Data Products: User Guide. (Version 1.2)*. https://asdc.larc.nasa.gov/documents/tempo/guide/TEMPO_Level-2-3_trace_gas_clouds_user_guide_V1.2.pdf

González Abad, G., Vasilkov, A., Seftor, C., Liu, X., & Chance, K. (2016). Smithsonian Astrophysical Observatory Ozone Mapping and Profiler Suite (SAO OMPS) formaldehyde retrieval. *Atmospheric Measurement Techniques*, *9*(7), 2797–2812. https://doi.org/10.5194/amt-9-2797-2016

Guenther, A. B., Jiang, X., Heald, C. L., Sakulyanontvittaya, T., Duhl, T., Emmons, L. K., & Wang, X. (2012). The Model of Emissions of Gases and Aerosols from Nature version 2.1 (MEGAN2.1): An extended and updated framework for modeling biogenic emissions. *Geoscientific Model Development*, *5*(6), 1471–1492. https://doi.org/10.5194/gmd-5-1471-2012

Hudman, R. C., Moore, N. E., Mebust, A. K., Martin, R. V., Russell, A. R., Valin, L. C., & Cohen, R. C. (2012). Steps towards a mechanistic model of global soil nitric oxide emissions: Implementation and space based-constraints. *Atmospheric Chemistry and Physics*, *12*(16), 7779–7795. https://doi.org/10.5194/acp-12-7779-2012

Janssens-Maenhout, G., Crippa, M., Guizzardi, D., Dentener, F., Muntean, M., Pouliot, G., Keating, T., Zhang, Q., Kurokawa, J., Wankmüller, R., Denier van der Gon, H., Kuenen, J. J. P., Klimont, Z., Frost, G., Darras, S., Koffi, B., & Li, M. (2015). HTAP_v2.2: A mosaic of regional and global emission grid maps for 2008 and 2010 to study hemispheric transport of air pollution. *Atmospheric Chemistry and Physics*, *15*(19), 11411–11432. https://doi.org/10.5194/acp-15-

11411-2015
Jin, X., Fiore, A. M., Murray, L. T., Valin, L. C., Lamsal, L. N., Duncan, B., Boersma, K. F., Smedt, I. D., Abad, G. G., Chance, K., & Tonnesen, G. S. (2017). Evaluating a Space-Based Indicator of Surface Ozone-NOx-VOC Sensitivity Over Midlatitude Source Regions and Application to Decadal Trends. *Journal of Geophysical Research: Atmospheres*, *122*(19), 10,439-10,461. https://doi.org/10.1002/2017JD026720
Jung, Y., González Abad, G., Nowlan, C. R., Chance, K., Liu, X., Torres, O., & Ahn, C. (2019). Explicit Aerosol Correction of OMI Formaldehyde Retrievals. *Earth and Space Science*, *6*(11), 2087–2105. https://doi.org/10.1029/2019EA000702
Keller, C. A., Knowland, K. E., Duncan, B. N., Liu, J., Anderson, D. C., Das, S., Lucchesi, R. A., Lundgren, E. W., Nicely, J. M., Nielsen, E., Ott, L. E., Saunders, E., Strode, S. A., Wales, P. A., Jacob, D. J., & Pawson, S. (2021). Description of the NASA GEOS Composition Forecast Modeling System GEOS-CF v1.0. *Journal of Advances in Modeling Earth Systems*, *13*(4), e2020MS002413. https://doi.org/10.1029/2020MS002413
Keller, C. A., Long, M. S., Yantosca, R. M., Da Silva, A. M., Pawson, S., & Jacob, D. J. (2014). HEMCO v1.0: A versatile, ESMF-compliant component for calculating emissions in atmospheric models. *Geoscientific Model Development*, *7*(4), 1409–1417. https://doi.org/10.5194/gmd-7-1409-2014
Kim, J., Jeong, U., Ahn, M.-H., Kim, J. H., Park, R. J., Lee, H., Song, C. H., Choi, Y.-S., Lee, K.-H., Yoo, J.-M., Jeong, M.-J., Park, S. K., Lee, K.-M., Song, C.-K., Kim, S.-W., Kim, Y. J., Kim, S.-W., Kim, M., Go, S., … Choi, Y. (2020). *New Era of Air Quality Monitoring from Space: Geostationary Environment Monitoring Spectrometer (GEMS)*. https://doi.org/10.1175/BAMS-D-18-0013.1
Kim, S., Chen, J., Cheng, T., Gindulyte, A., He, J., He, S., Li, Q., Shoemaker, B. A., Thiessen, P. A., Yu, B., Zaslavsky, L., Zhang, J., & Bolton, E. E. (2019). PubChem 2019 update: Improved access to chemical data. *Nucleic Acids Research*, *47*(D1), D1102–D1109. https://doi.org/10.1093/nar/gky1033
Knowland, K. E., Keller, C. A., & Lucchesi, R. A. (2022). *File specification for GEOS-CF products*. GMAO Office Note. https://gmao.gsfc.nasa.gov/pubs/docs/Knowland1204.pdf
Knowland, K. E., Keller, C. A., Wales, P. A., Wargan, K., Coy, L., Johnson, M. S., Liu, J., Lucchesi, R. A., Eastham, S. D., Fleming, E., Liang, Q., Leblanc, T., Livesey, N. J., Walker, K. A., Ott, L. E., & Pawson, S. (2022). NASA GEOS Composition Forecast Modeling System GEOS-CF v1.0: Stratospheric Composition. *Journal of Advances in Modeling Earth Systems*, *14*(6), e2021MS002852. https://doi.org/10.1029/2021MS002852
Kokaly, R. F., Clark, R. N., Swayze, G. A., Livo, K. E., Hoefen, T. M., Pearson, N. C., Wise, R. A., Benzel, W. M., Lowers, H. A., Driscoll, R. L., & Klein, A. J. (2017). *USGS Spectral Library Version 7* (Report No. 1035; Data Series, p. 68). USGS Publications Warehouse. https://doi.org/10.3133/ds1035
Koster, R. D., Darmenov, A. S., & da Silva, A. M. (2015). *The Quick Fire Emissions Dataset (QFED): Documentation of Versions 2.1, 2.2 and 2.4: Technical Report Series on Global Modeling and Data Assimilation - Volume 38* (No. NASA/TM-2015-104606 /Vol. 38). https://ntrs.nasa.gov/citations/20180005253
Kwon, H.-A., González Abad, G., Chan Miller, C., Hall, K. R., Nowlan, C. R., O'Sullivan, E., Wang, H., Chong, H., Ayazpour, Z., Liu, X., & Chance, K. (2024). Updated OMI Glyoxal Column Measurements Using Collection 4 Level 1B Radiances. *Earth and Space Science*, *11*(9), e2024EA003705. https://doi.org/10.1029/2024EA003705
Kwon, H.-A., Park, R. J., González Abad, G., Chance, K., Kurosu, T. P., Kim, J., De Smedt, I., Van Roozendael, M., Peters, E., & Burrows, J. (2019). Description of a formaldehyde retrieval algorithm for the Geostationary Environment Monitoring Spectrometer (GEMS). *Atmospheric Measurement Techniques*, *12*(7), 3551–3571. https://doi.org/10.5194/amt-12-3551-2019
Kwon, H.-A., Park, R. J., Jeong, J. I., Lee, S., González Abad, G., Kurosu, T. P., Palmer, P. I., & Chance, K. (2017). Sensitivity of formaldehyde (HCHO) column measurements from a geostationary

satellite to temporal variation of the air mass factor in East Asia. *Atmospheric Chemistry and Physics*, *17*(7), 4673–4686. https://doi.org/10.5194/acp-17-4673-2017

Lamsal, L. N., Krotkov, N. A., Vasilkov, A., Marchenko, S., Qin, W., Yang, E.-S., Fasnacht, Z., Joiner, J., Choi, S., Haffner, D., Swartz, W. H., Fisher, B., & Bucsela, E. (2021). Ozone Monitoring Instrument (OMI) Aura nitrogen dioxide standard product version 4.0 with improved surface and cloud treatments. *Atmospheric Measurement Techniques*, *14*(1), 455–479. https://doi.org/10.5194/amt-14-455-2021

Lee, G. T., Park, R. J., Kwon, H.-A., Ha, E. S., Lee, S. D., Shin, S., Ahn, M.-H., Kang, M., Choi, Y.-S., Kim, G., Lee, D.-W., Kim, D.-R., Hong, H., Langerock, B., Vigouroux, C., Lerot, C., Hendrick, F., Pinardi, G., De Smedt, I., … Kim, J. (2024). First evaluation of the GEMS formaldehyde product against TROPOMI and ground-based column measurements during the in-orbit test period. *Atmospheric Chemistry and Physics*, *24*(8), 4733–4749. https://doi.org/10.5194/acp-24-4733-2024

Lee, Y.-N., Zhou, X., Kleinman, L. I., Nunnermacker, L. J., Springston, S. R., Daum, P. H., Newman, L., Keigley, W. G., Holdren, M. W., Spicer, C. W., Young, V., Fu, B., Parrish, D. D., Holloway, J., Williams, J., Roberts, J. M., Ryerson, T. B., & Fehsenfeld, F. C. (1998). Atmospheric chemistry and distribution of formaldehyde and several multioxygenated carbonyl compounds during the 1995 Nashville/Middle Tennessee Ozone Study. *Journal of Geophysical Research: Atmospheres*, *103*(D17), 22449–22462. https://doi.org/10.1029/98JD01251

Leitão, J., Richter, A., Vrekoussis, M., Kokhanovsky, A., Zhang, Q. J., Beekmann, M., & Burrows, J. P. (2010). On the improvement of NO_2 satellite retrievals – aerosol impact on the airmass factors. *Atmospheric Measurement Techniques*, *3*(2), 475–493. https://doi.org/10.5194/amt-3-475-2010

Levelt, P. F., Oord, G. H. J. van den, Dobber, M. R., Malkki, A., Visser, H., Vries, J. de, Stammes, P., Lundell, J. O. V., & Saari, H. (2006). The ozone monitoring instrument. *IEEE Transactions on Geoscience and Remote Sensing*, *44*(5), 1093–1101. https://doi.org/10.1109/TGRS.2006.872333

Li, C., Joiner, J., Krotkov, N. A., & Dunlap, L. (2015). A new method for global retrievals of HCHO total columns from the Suomi National Polar-orbiting Partnership Ozone Mapping and Profiler Suite. *Geophysical Research Letters*, *42*(7), 2515–2522. https://doi.org/10.1002/2015GL063204

Liu, C., Liu, X., Kowalewski, M. G., Janz, S. J., González Abad, G., Pickering, K. E., Chance, K., & Lamsal, L. N. (2015). Characterization and verification of ACAM slit functions for trace-gas retrievals during the 2011 DISCOVER-AQ flight campaign. *Atmos. Meas. Tech.*, *8*(2), 751–759. https://doi.org/10.5194/amt-8-751-2015

Liu, F., Choi, S., Li, C., Fioletov, V. E., McLinden, C. A., Joiner, J., Krotkov, N. A., Bian, H., Janssens-Maenhout, G., Darmenov, A. S., & da Silva, A. M. (2018). A new global anthropogenic SO_2 emission inventory for the last decade: A mosaic of satellite-derived and bottom-up emissions. *Atmospheric Chemistry and Physics*, *18*(22), 16571–16586. https://doi.org/10.5194/acp-18-16571-2018

Liu, X., Bhartia, P. K., Chance, K., Spurr, R. J. D., & Kurosu, T. P. (2010). Ozone profile retrievals from the Ozone Monitoring Instrument. *Atmos. Chem. Phys.*, *10*(5), 2521–2537. https://doi.org/10.5194/acp-10-2521-2010

Logan, J. A., Prather, M. J., Wofsy, S. C., & McElroy, M. B. (1981). Tropospheric chemistry: A global perspective. *Journal of Geophysical Research: Oceans*, *86*(C8), 7210–7254. https://doi.org/10.1029/JC086iC08p07210

Lorente, A., Boersma, K. F., Yu, H., Dörner, S., Hilboll, A., Richter, A., Liu, M., Lamsal, L. N., Barkley, M., Smedt, I. D., Roozendael, M. V., Wang, Y., Wagner, T., Beirle, S., Lin, J. T., Krotkov, N., Stammes, P., Wang, P., Eskes, H. J., & Krol, M. (2017). Structural uncertainty in air mass factor calculation for NO2 and HCHO satellite retrievals. *Atmospheric Measurement Techniques*, *10*(3), 759–782. https://doi.org/10.5194/amt-10-759-2017

Lucchesi, R. (2013, January 15). *File Specification for GEOS-5 FP-IT (Forward Processing for Instrument Teams)*. https://ntrs.nasa.gov/citations/20150001438

Mao, J., Paulot, F., Jacob, D. J., Cohen, R. C., Crounse, J. D., Wennberg, P. O., Keller, C. A., Hudman,

R. C., Barkley, M. P., & Horowitz, L. W. (2013). Ozone and organic nitrates over the eastern United States: Sensitivity to isoprene chemistry. *Journal of Geophysical Research: Atmospheres*, *118*(19), 11,256-11,268. https://doi.org/10.1002/jgrd.50817

Marais, E. A., Jacob, D. J., Jimenez, J. L., Campuzano-Jost, P., Day, D. A., Hu, W., Krechmer, J., Zhu, L., Kim, P. S., Miller, C. C., Fisher, J. A., Travis, K., Yu, K., Hanisco, T. F., Wolfe, G. M., Arkinson, H. L., Pye, H. O. T., Froyd, K. D., Liao, J., & McNeill, V. F. (2016). Aqueous-phase mechanism for secondary organic aerosol formation from isoprene: Application to the southeast United States and co-benefit of SO_2 emission controls. *Atmospheric Chemistry and Physics*, *16*(3), 1603–1618. https://doi.org/10.5194/acp-16-1603-2016

Marais, E. A., Jacob, D. J., Kurosu, T. P., Chance, K., Murphy, J. G., Reeves, C., Mills, G., Casadio, S., Millet, D. B., Barkley, M. P., Paulot, F., & Mao, J. (2012). Isoprene emissions in Africa inferred from OMI observations of formaldehyde columns. *Atmospheric Chemistry and Physics*, *12*(14), 6219–6235. https://doi.org/10.5194/acp-12-6219-2012

Martin, R. V., Chance, K., Jacob, D. J., Kurosu, T. P., Spurr, R. J. D., Bucsela, E., Gleason, J. F., Palmer, P. I., Bey, I., Fiore, A. M., Li, Q., Yantosca, R. M., & Koelemeijer, R. B. A. (2002). An improved retrieval of tropospheric nitrogen dioxide from GOME. *Journal of Geophysical Research: Atmospheres*, *107*(D20), ACH 9-1-ACH 9-21. https://doi.org/10.1029/2001JD001027

Munger, J., Jacob, D., Daube, B., Horowitz, L., Keene, W., & Heikes, B. (1995). Formaldehyde, glyoxal, and methylglyoxal in air and cloudwater at a rural mountain site in central Virginia. *Journal of Geophysical Research*, *100*, 9325–9333. https://doi.org/10.1029/95JD00508

Munro, R., Lang, R., Klaes, D., Poli, G., Retscher, C., Lindstrot, R., Huckle, R., Lacan, A., Grzegorski, M., Holdak, A., Kokhanovsky, A., Livschitz, J., & Eisinger, M. (2016). The GOME-2 instrument on the Metop series of satellites: Instrument design, calibration, and level 1 data processing – an overview. *Atmospheric Measurement Techniques*, *9*(3), 1279–1301. https://doi.org/10.5194/amt-9-1279-2016

Murray, L. T., Jacob, D. J., Logan, J. A., Hudman, R. C., & Koshak, W. J. (2012). Optimized regional and interannual variability of lightning in a global chemical transport model constrained by LIS/OTD satellite data. *Journal of Geophysical Research: Atmospheres*, *117*(D20). https://doi.org/10.1029/2012JD017934

National Research Council. (2007). *Earth Science and Applications from Space: National Imperatives for the Next Decade and Beyond*. National Academies Press. https://doi.org/10.17226/11820

Noël, S., Bramstedt, K., Bovensmann, H., Gerilowski, K., Burrows, J. P., Standfuss, C., Dufour, E., & Veihelmann, B. (2012). Quantification and mitigation of the impact of scene inhomogeneity on Sentinel-4 UVN UV-VIS retrievals. *Atmospheric Measurement Techniques*, *5*(6), 1319–1331. https://doi.org/10.5194/amt-5-1319-2012

Nowlan, C. R., González Abad, G., Kwon, H.-A., Ayazpour, Z., Chan Miller, C., Chance, K., Chong, H., Liu, X., O'Sullivan, E., Wang, H., Zhu, L., De Smedt, I., Jaross, G., Seftor, C., & Sun, K. (2023). Global Formaldehyde Products From the Ozone Mapping and Profiler Suite (OMPS) Nadir Mappers on Suomi NPP and NOAA-20. *Earth and Space Science*, *10*(5), e2022EA002643. https://doi.org/10.1029/2022EA002643

Nowlan, C. R., Liu, X., Chance, K., Cai, Z., Kurosu, T. P., Lee, C., & Martin, R. V. (2011). Retrievals of sulfur dioxide from the Global Ozone Monitoring Experiment 2 (GOME-2) using an optimal estimation approach: Algorithm and initial validation. *Journal of Geophysical Research: Atmospheres*, *116*(D18). https://doi.org/10.1029/2011JD015808

Nowlan, C. R., Liu, X., Janz, S. J., Kowalewski, M. G., Chance, K., Follette-Cook, M. B., Fried, A., González Abad, G., Herman, J. R., Judd, L. M., Kwon, H.-A., Loughner, C. P., Pickering, K. E., Richter, D., Spinei, E., Walega, J., Weibring, P., & Weinheimer, A. J. (2018). Nitrogen dioxide and formaldehyde measurements from the GEOstationary Coastal and Air Pollution Events (GEO-CAPE) Airborne Simulator over Houston, Texas. *Atmospheric Measurement Techniques*, *11*(11), 5941–5964. https://doi.org/10.5194/amt-11-5941-2018

Nowlan, C. R., Liu, X., Leitch, J. W., Chance, K., González Abad, G., Liu, C., Zoogman, P., Cole, J.,

Delker, T., Good, W., Murcray, F., Ruppert, L., Soo, D., Follette-Cook, M. B., Janz, S. J., Kowalewski, M. G., Loughner, C. P., Pickering, K. E., Herman, J. R., … Al-Saadi, J. A. (2016). Nitrogen dioxide observations from the Geostationary Trace gas and Aerosol Sensor Optimization (GeoTASO) airborne instrument: Retrieval algorithm and measurements during DISCOVER-AQ Texas 2013. *Atmos. Meas. Tech.*, *9*(6), 2647–2668. https://doi.org/10.5194/amt-9-2647-2016

Oda, T., Maksyutov, S., & Andres, R. J. (2018). The Open-source Data Inventory for Anthropogenic CO_2, version 2016 (ODIAC2016): A global monthly fossil fuel CO_2 gridded emissions data product for tracer transport simulations and surface flux inversions. *Earth System Science Data*, *10*(1), 87–107. https://doi.org/10.5194/essd-10-87-2018

Palmer, P. I., Jacob, D. J., Chance, K., Martin, R. V., Spurr, R. J. D., Kurosu, T. P., Bey, I., Yantosca, R., Fiore, A., & Li, Q. (2001). Air mass factor formulation for spectroscopic measurements from satellites: Application to formaldehyde retrievals from the Global Ozone Monitoring Experiment. *Journal of Geophysical Research: Atmospheres*, *106*(D13), 14539–14550. https://doi.org/10.1029/2000JD900772

Parrella, J. P., Chance, K., Salawitch, R. J., Canty, T., Dorf, M., & Pfeilsticker, K. (2013). New retrieval of BrO from SCIAMACHY limb: An estimate of the stratospheric bromine loading during April 2008. *Atmos. Meas. Tech.*, *6*(10), 2549–2561. https://doi.org/10.5194/amt-6-2549-2013

Parrella, J. P., Jacob, D. J., Liang, Q., Zhang, Y., Mickley, L. J., Miller, B., Evans, M. J., Yang, X., Pyle, J. A., Theys, N., & Van Roozendael, M. (2012). Tropospheric bromine chemistry: Implications for present and pre-industrial ozone and mercury. *Atmospheric Chemistry and Physics*, *12*(15), 6723–6740. https://doi.org/10.5194/acp-12-6723-2012

Qin, W., Fasnacht, Z., Haffner, D., Vasilkov, A., Joiner, J., Krotkov, N., Fisher, B., & Spurr, R. (2019). A geometry-dependent surface Lambertian-equivalent reflectivity product at 466 nm for UV/Vis retrievals: Part I. Evaluation over land surfaces using measurements from OMI. *Atmospheric Measurement Techniques Discussions*, 1–31. https://doi.org/10.5194/amt-2018-327

Schaaf, C., & Wang, Z. (2015a). MCD43C1 MODIS/Terra+Aqua BRDF/Albedo Model Parameters Daily L3 Global 0.05Deg CMG V006. *Distributed by NASA EOSDIS Land Processes DAAC*. https://doi.org/10.5067/MODIS/MCD43C1.006

Schaaf, C., & Wang, Z. (2015b). MCD43C2 MODIS/Terra+Aqua BRDF/Albedo Snow-Free Model Parameters Daily L3 Global 0.05Deg CMG V006. *Distributed by NASA EOSDIS Land Processes DAAC*. https://doi.org/10.5067/MODIS/MCD43C2.006

Schultz, M. G., Heil, A., Hoelzemann, J. J., Spessa, A., Thonicke, K., Goldammer, J. G., Held, A. C., Pereira, J. M. C., & van het Bolscher, M. (2008). Global wildland fire emissions from 1960 to 2000. *Global Biogeochemical Cycles*, *22*(2). https://doi.org/10.1029/2007GB003031

Serdyuchenko, A., Gorshelev, V., Weber, M., Chehade, W., & Burrows, J. P. (2014). High spectral resolution ozone absorption cross-sections – Part 2: Temperature dependence. *Atmospheric Measurement Techniques*, *7*(2), 625–636. https://doi.org/10.5194/amt-7-625-2014

Sherwen, T., Schmidt, J. A., Evans, M. J., Carpenter, L. J., Großmann, K., Eastham, S. D., Jacob, D. J., Dix, B., Koenig, T. K., Sinreich, R., Ortega, I., Volkamer, R., Saiz-Lopez, A., Prados-Roman, C., Mahajan, A. S., & Ordóñez, C. (2016). Global impacts of tropospheric halogens (Cl, Br, I) on oxidants and composition in GEOS-Chem. *Atmospheric Chemistry and Physics*, *16*(18), 12239–12271. https://doi.org/10.5194/acp-16-12239-2016

Sioris, C. E., Kurosu, T. P., Martin, R. V., & Chance, K. (2004). Stratospheric and tropospheric NO2 observed by SCIAMACHY: First results. *Advances in Space Research*, *34*(4), 780–785. https://doi.org/10.1016/j.asr.2003.08.066

Souri, A. H., Nowlan, C. R., Wolfe, G. M., Lamsal, L. N., Chan Miller, C. E., Abad, G. G., Janz, S. J., Fried, A., Blake, D. R., Weinheimer, A. J., Diskin, G. S., Liu, X., & Chance, K. (2020). Revisiting the effectiveness of HCHO/NO2 ratios for inferring ozone sensitivity to its precursors using high resolution airborne remote sensing observations in a high ozone episode during the KORUS-AQ campaign. *Atmospheric Environment*, *224*, 117341.

https://doi.org/10.1016/j.atmosenv.2020.117341
Spurr, R. J. D. (2006). VLIDORT: A linearized pseudo-spherical vector discrete ordinate radiative transfer code for forward model and retrieval studies in multilayer multiple scattering media. *Journal of Quantitative Spectroscopy and Radiative Transfer*, *102*(2), 316–342. https://doi.org/10.1016/j.jqsrt.2006.05.005
Stavrakou, T., Müller, J.-F., De Smedt, I., Van Roozendael, M., van der Werf, G. R., Giglio, L., & Guenther, A. (2009). Evaluating the performance of pyrogenic and biogenic emission inventories against one decade of space-based formaldehyde columns. *Atmospheric Chemistry and Physics*, *9*(3), 1037–1060. https://doi.org/10.5194/acp-9-1037-2009
Stavrakou, T., Müller, J.-F., Smedt, I. D., Roozendael, M. V., Werf, G. R. van der, Giglio, L., & Guenther, A. (2009). Evaluating the performance of pyrogenic and biogenic emission inventories against one decade of space-based formaldehyde columns. *Atmospheric Chemistry and Physics*, *9*(3), 1037–1060. https://doi.org/10.5194/acp-9-1037-2009
Su, W., Liu, C., Hu, Q., Zhang, C., Liu, H., Xia, C., Zhao, F., Liu, T., Lin, J., & Chen, Y. (2022). First global observation of tropospheric formaldehyde from Chinese GaoFen-5 satellite: Locating source of volatile organic compounds. *Environmental Pollution*, *297*, 118691. https://doi.org/10.1016/j.envpol.2021.118691
Suleiman, R. M., Chance, K., Liu, X., González Abad, G., Kurosu, T. P., Hendrick, F., & Theys, N. (2018). OMI total bromine monoxide (OMBRO) data product: Algorithm, retrieval and measurement comparisons. *Atmospheric Measurement Techniques Discussions*, 1–33. https://doi.org/10.5194/amt-2018-1
Sun, K., Liu, X., Huang, G., González Abad, G., Cai, Z., Chance, K., & Yang, K. (2017). Deriving the slit functions from OMI solar observations and its implications for ozone-profile retrieval. *Atmos. Meas. Tech.*, *10*(10), 3677–3695. https://doi.org/10.5194/amt-10-3677-2017
Swenberg, J. A., Moeller, B. C., Lu, K., Rager, J. E., Fry, R., & Starr, T. B. (2013). Formaldehyde Carcinogenicity Research: 30 Years and Counting for Mode of Action, Epidemiology, and Cancer Risk Assessment. *Toxicologic Pathology*, *41*(2), 181–189. https://doi.org/10.1177/0192623312466459
TEMPO Validation Team. (2023). *Tropospheric Emissions: Monitoring of Pollution (TEMPO)—Level 2 Science Data Product Validation Plan*. https://tempo.si.edu/documents/SAO-DRD-11_TEMPO%20Science%20Validation_Plan_Baseline.pdf
TEMPO Validation Team. (2025). *Validation and Quality Assessment of the TEMPO Level-2 Trace Gas Products*. TBD
Thomas, W., Hegels, E., Slijkhuis, S., Spurr, R., & Chance, K. (1998). Detection of biomass burning combustion products in Southeast Asia from backscatter data taken by the GOME Spectrometer. *Geophysical Research Letters*, *25*(9), 1317–1320. https://doi.org/10.1029/98GL01087
Tilstra, L. G., Tuinder, O. N. E., Wang, P., & Stammes, P. (2017). Surface reflectivity climatologies from UV to NIR determined from Earth observations by GOME-2 and SCIAMACHY. *Journal of Geophysical Research: Atmospheres*, *122*(7), 4084–4111. https://doi.org/10.1002/2016JD025940
U.S. National Ice Center. (2008). IMS Daily Northern Hemisphere Snow and Ice Analysis at 4 km and 24 km Resolution. *[1997-Present]. Boulder, Colorado USA. NSIDC: National Snow and Ice Data Center*. https://doi.org/10.7265/N52R3PMC
Valin, L. C., Fiore, A. M., Chance, K., & Abad, G. G. (2016). The role of OH production in interpreting the variability of CH2O columns in the southeast U.S. *Journal of Geophysical Research: Atmospheres*, *121*(1), 478–493. https://doi.org/10.1002/2015JD024012
van der Gon, H. D., Hendriks, C., Kuene, J., Arjo, S., & Visschedijk, A. (2011). *TNO Report: Description of current temporal emission patterns and sensitivity*. https://atmosphere.copernicus.eu/sites/default/files/2019-07/MACC_TNO_del_1_3_v2.pdf
Vandaele, A. C., Hermans, C., Simon, P. C., Carleer, M., Colin, R., Fally, S., Mérienne, M. F., Jenouvrier, A., & Coquart, B. (1998). Measurements of

the NO2 absorption cross-section from 42 000 cm-1 to 10 000 cm-1 (238–1000 nm) at 220 K and 294 K. *Journal of Quantitative Spectroscopy and Radiative Transfer*, *59*(3), 171–184. https://doi.org/10.1016/S0022-4073(97)00168-4

Veefkind, J. P., Aben, I., McMullan, K., Förster, H., de Vries, J., Otter, G., Claas, J., Eskes, H. J., de Haan, J. F., Kleipool, Q., van Weele, M., Hasekamp, O., Hoogeveen, R., Landgraf, J., Snel, R., Tol, P., Ingmann, P., Voors, R., Kruizinga, B., … Levelt, P. F. (2012). TROPOMI on the ESA Sentinel-5 Precursor: A GMES mission for global observations of the atmospheric composition for climate, air quality and ozone layer applications. *Remote Sensing of Environment*, *120*, 70–83. 85.67. https://doi.org/10.1016/j.rse.2011.09.027

Voors, R., Dobber, M., Dirksen, R., & Levelt, P. (2006). Method of calibration to correct for cloud-induced wavelength shifts in the Aura satellite's Ozone Monitoring Instrument. *Applied Optics*, *45*(15), 3652–3658. https://doi.org/10.1364/AO.45.003652

Wang, H., Nowlan, C., González Abad, G., Chong, H., Hou, W., Houck, J., Liu, X., Chance, K., Yang, E.-S., Vasilkov, A., Joiner, J., Qin, W., Fasnacht, Z., Knowland, K. E., Chan Miller, C., Spurr, R., Flittner, D. E., Carr, J. L., Suleiman, R. M., … Fitzmaurice, J. A. (2025). Algorithm theoretical basis for Version 3 TEMPO O_2-O_2 cloud product. *Earth and Space Science*, *12*, e2024EA004165. https://doi.org/10.1029/2024EA004165

Wang, H., Souri, A. H., González Abad, G., Liu, X., & Chance, K. (2019). Ozone Monitoring Instrument (OMI) Total Column Water Vapor version 4 validation and applications. *Atmospheric Measurement Techniques*, *12*(9), 5183–5199. https://doi.org/10.5194/amt-12-5183-2019

Wargan, K., Pawson, S., Olsen, M. A., Witte, J. C., Douglass, A. R., Ziemke, J. R., Strahan, S. E., & Nielsen, J. E. (2015). The global structure of upper troposphere-lower stratosphere ozone in GEOS-5: A multiyear assimilation of EOS Aura data. *Journal of Geophysical Research: Atmospheres*, *120*(5), 2013–2036. https://doi.org/10.1002/2014JD022493

Wilmouth, D. M., Hanisco, T. F., Donahue, N. M., & Anderson, J. G. (1999). Fourier Transform Ultraviolet Spectroscopy of the A 2Π3/2 ← X 2Π3/2 Transition of BrO. *The Journal of Physical Chemistry A*, *103*(45), 8935–8945. https://doi.org/10.1021/jp991651o

Wittrock, F., Richter, A., Oetjen, H., Burrows, J. P., Kanakidou, M., Myriokefalitakis, S., Volkamer, R., Beirle, S., Platt, U., & Wagner, T. (2006). Simultaneous global observations of glyoxal and formaldehyde from space. *Geophysical Research Letters*, *33*(16). https://doi.org/10.1029/2006GL026310

Wolfe, G. M., Nicely, J. M., Clair, J. M. S., Hanisco, T. F., Liao, J., Oman, L. D., Brune, W. B., Miller, D., Thames, A., Abad, G. G., Ryerson, T. B., Thompson, C. R., Peischl, J., McKain, K., Sweeney, C., Wennberg, P. O., Kim, M., Crounse, J. D., Hall, S. R., … Dean-Day, J. (2019). Mapping hydroxyl variability throughout the global remote troposphere via synthesis of airborne and satellite formaldehyde observations. *Proceedings of the National Academy of Sciences*, *116*(23), 11171–11180. https://doi.org/10.1073/pnas.1821661116

Zhang, H., Li, J., Ying, Q., Guven, B. B., & Olaguer, E. P. (2018). Source apportionment of formaldehyde during TexAQS 2006 using a source-oriented chemical transport model. *Journal of Geophysical Research: Atmospheres*, 1525–1535. https://doi.org/10.1002/jgrd.50197@10.1002/(ISSN)2169-8996.SHARP1

Zhou, Y., Brunner, D., Boersma, K. F., Dirksen, R., & Wang, P. (2009). An improved tropospheric NO_2 retrieval for OMI observations in the vicinity of mountainous terrain. *Atmospheric Measurement Techniques*, *2*(2), 401–416. https://doi.org/10.5194/amt-2-401-2009

Zhu, L., Jacob, D. J., Keutsch, F. N., Mickley, L. J., Scheffe, R., Strum, M., González Abad, G., Chance, K., Yang, K., Rappenglück, B., Millet, D. B., Baasandorj, M., Jaeglé, L., & Shah, V. (2017). Formaldehyde (HCHO) As a Hazardous Air Pollutant: Mapping Surface Air Concentrations from Satellite and Inferring Cancer Risks in the United States. *Environmental Science & Technology*, *51*(10), 5650–5657. https://doi.org/10.1021/acs.est.7b01356

Zhu, L., Jacob, D. J., Mickley, L. J., Marais, E. A., Cohan, D. S., Yoshida, Y., Duncan, B. N., Abad, G.

G., & Chance, K. V. (2014). Anthropogenic emissions of highly reactive volatile organic compounds in eastern Texas inferred from oversampling of satellite (OMI) measurements of HCHO columns. *Environmental Research Letters*, *9*(11), 114004. https://doi.org/10.1088/1748-9326/9/11/114004

Zhu, L., Mickley, L. J., Jacob, D. J., Marais, E. A., Sheng, J., Hu, L., Abad, G. G., & Chance, K. (2017). Long-term (2005–2014) trends in formaldehyde (HCHO) columns across North America as seen by the OMI satellite instrument: Evidence of changing emissions of volatile organic compounds. *Geophysical Research Letters*, *44*(13), 7079–7086. https://doi.org/10.1002/2017GL073859

Zoogman, P., Liu, X., Chance, K., Sun, Q., Schaaf, C., Mahr, T., & Wagner, T. (2016). A climatology of visible surface reflectance spectra. *Journal of Quantitative Spectroscopy and Radiative Transfer*, *180*, 39–46. https://doi.org/10.1016/j.jqsrt.2016.04.003

Zoogman, P., Liu, X., Suleiman, R. M., Pennington, W. F., Flittner, D. E., Al-Saadi, J. A., Hilton, B. B., Nicks, D. K., Newchurch, M. J., Carr, J. L., Janz, S. J., Andraschko, M. R., Arola, A., Baker, B. D., Canova, B. P., Chan Miller, C., Cohen, R. C., Davis, J. E., Dussault, M. E., … Chance, K. (2017). Tropospheric emissions: Monitoring of pollution (TEMPO). *Journal of Quantitative Spectroscopy and Radiative Transfer*, *186*, 17–39. 85.68. https://doi.org/10.1016/j.jqsrt.2016.05.008